1   **Revision 1**

2

3   **Mineralogy of the 2019 Aguas Zarcas (CM2) carbonaceous chondrite**
4   **meteorite fall**

5

6   Laurence A.J. Garvie

7   Center for Meteorite Studies, Arizona State University, Tempe, Arizona 85287–6004,
8   USA

9

10   **ABSTRACT**

11   The 2019 Aguas Zarcas CM2 meteorite is the most significant carbonaceous chondrite
12   CM2 fall since Murchison in 1969. Samples collected immediately following the fall, and
13   studied here, provide the rare opportunity to analyze the bulk mineralogy of a CM2 largely
14   free of terrestrial contamination. Bulk samples were analyzed by powder X-ray diffraction
15   (XRD), thermal gravimetric (TG) analysis, evolved gas analysis (EGA), and scanning
16   electron microscopy (SEM) with an electron-probe micro-analyzer (EPMA). Water-
17   extracted salts were analyzed by XRD. In hand specimen, the stones are brecciated and
18   dominated by chondrule-rich and –poor lithologies, and locally, a matrix-rich lithology.
19   Powder XRD patterns from multiple stones are dominated by reflections from serpentine
20   group minerals, on which are superimposed reflections for ferrotochilinite, 1:1 regularly
21   interstratified ferrotochilinite/cronstedtite, anhydrous silicates, calcite, pentlandite,
22   pyrrhotite, and minor phases. Reflections for magnetite are present only from a metal-rich
23   breccia clast. The serpentine XRD reflections from the chondrule-rich and –poor
24   lithologies match those from 1T cronstedtite, whereas those from the matrix-rich lithology
25   match the 1M polytype. Patterns with the 1M polytype also show a distinct low-angle
26   scattering to the serpentine basal reflection centered near 8.6 Å, the origin of which is
27   obscure. Further matching of the known serpentines to the Aguas Zarcas data shows that
28   cronstedtite accounts for a subordinate amount of the clays, and at least three other
29   chemically and structurally distinct serpentines are likely present. A typical fragment of
30   Aguas Zarcas yielded 0.6 wt% water-extractable salts. The powder XRD pattern of the
31   dried water extract shows reflections for halite - NaCl; chlorartinite –
32     $Mg_2(CO_3)(OH)Cl.2H_2O$; thenardite – Na_2SO_4; and, sodium chlorate – $NaClO_4$. The TG
33   mass losses of 11.4 to 14.7 wt% are consistent with other CM2 chondrites. The gases
34   detected by EGA are dominated by H_2O and CO_2, largely derived from the dehydroxylation
35   and decomposition of serpentine and calcite, respectively. Also detected are gases with
36   masses matching SO_2/S_2 and H_2S, which are primarily released below 480° C, and a mass
37   of 30, which matches the molecular weight of formaldehyde and ethane, shows a maximum
38   at 376° C. These organic gases likely derive from the pyrolysis of indigenous organic
39   matter. Taken together, the mm-scale mineralogical study of Aguas Zarcas reveals a
40   complex breccia dominated by CM2-like clasts. The detailed study of this meteorite,
41   together with similar studies from a range of carbonaceous chondrites, provides the
42   foundations for studying and interpreting the samples returned from the NASA OSIRIS-
43   REx and JAXA Hayabusa2 missions.

44

45
46   **INTRODUCTION**

47   Around 21:07 local time on the 23rd of April, 2019, a large fireball over Costa Rica

48   dropped multiple kilograms of meteorites over the Alajuela province in Costa Rica.

49   Hundreds of stones were collected in and around the town of Aguas Zarcas (Garvie et al.

50   2019; Lücke et al. 2019). Approximately 11 kg of stones were collected prior to rains

51   hitting the fall site. The meteorite hunter Michael Farmer provided nearly 5 kg of pristine,

52   pre-rain material for study to the Center for Meteorite Studies (CMS) at Arizona State

53   University (ASU). Initial classification work (Garvie et al. 2019) shows that this fall

54   mineralogically, petrographically, and isotopically overlaps with the CM2 carbonaceous

55   chondrites. This meteorite was approved by the Nomenclature Committee of The

56   Meteoritical Society as Aguas Zarcas (CM2) (Garvie et al. 2019).

57   Aguas Zarcas is a breccia containing both chondrule-poor and -rich lithologies

58   (Garvie et al. 2019; Kouvatsis and Cartwright 2020), and some stones contain clasts that

59   are metal rich and have O isotopes that do not overlap with the CM field (Kerraouch et al.

60   2020). Preliminary analysis shows a phyllosilicate abundance of ~75 to 85 vol% (Davidson

61   et al. 2020; Takir et al. 2020). The bulk mineralogy from a fragment shows a total

62   phyllosilicate content of 77.8%, dominated by cronstedtite (37%) and Mg/Fe serpentine

63   (40%) (Takir et al. 2020). The C, H, and N elemental data are within the range of other

64   CM2 chondrites (Vacher et al. 2020), with 2.13 wt% C, 0.868 wt% H, and 0.098 wt% N.

65   In addition, the recent fall and pristine nature of this stone has motivated a flurry of organic

66   analyses (Aponte et al. 2020; Glavin et al. 2020; Kebukawa et al. 2020; Pizzarello et al.

67   2020). Interestingly, while the samples analyzed by Pizzarello et al. 2020) contained little

68   if any measurable ammonia, amino acids and amines, the pieces analyzed by Glavin et al.

69   (2020) contained a range of amino acids, including α-AIB and isovaline. These amino

70   acids are rare in biology, and their isotopic composition is consistent with their

71   extraterrestrial origin. These disparate results for the same meteorite suggest a breccia with

72   considerable organic heterogeneity.

73   Carbonaceous chondrite (CC) meteorites are stony fragments of primitive

74   asteroidal bodies with near bulk Solar compositions (Anders and Grevesse 1989; Wasson

75   and Kallemyn 1988; Greenwood et al. 2020). The C class of chondrites is divided into eight

76   well-established groups, with distinct bulk compositional and O isotopic characteristics,

77   i.e., CI, CM, CR, CV, CO, CK, CH, and CB (Brearley and Jones 1998; Weisberg et al.

78   2006), the recently proposed CY group (King et al. 2019), and many ungrouped individual

79   meteorites. Many of the CC meteorites derive from asteroidal bodies that have experienced

80   various degrees of aqueous processing, where H_2O reacted with anhydrous silicates

81   forming phyllosilicates (e.g., Brearley 2006).

82   The CM group, where M refers to the Mighei chemical group of carbonaceous

83   chondrites, contains a diverse suite of meteorites that have undergone various degrees of

84   aqueous alteration and brecciation on their parent bodies (Metzler et al. 1992; Brearley and

85   Jones 1998). The CM2 group are classified as petrologic type 2, and indicates that the
86   matrices of these meteorites are essentially fully hydrated, with various degrees of
87   hydration of the chondrules (Brearley and Jones 1998; Brearley 2006). The CM2
88   meteorites contain 56 to 89 vol% phyllosilicates (Howard et al. 2009; 2015), which is
89   dominated by serpentines. These phyllosilicates are primarily present as a matrix that hosts
90   chondrules, CAIs, anhydrous mineral fragments, and commonly occurring minor phases
91   including calcite, magnetite, and sulfides. A few rare CM1 meteorites have been described,
92   in which close to 100% of the meteorite consists of hydrated minerals, e.g., Moapa Valley
93   (Irving et al. 2009). Recently, the Kolang (CM1/2) meteorite fall was recovered and
94   classified (Garvie et al. 2020). This meteorite contains areas with chondrules completely
95   replaced by hydrous silicates and intimately associated and mixed with chondrules and
96   olivine fragments partially replaced by hydrous phases (CM1/2), to areas more typical of
97   CM2 meteorites.

98   The CM2 meteorites are of interest, in part, because of their diverse extraterrestrial
99   organic chemistry and abundance of hydrated minerals, which together may hold clues to
100 the origin of water and life on Earth. The carbonaceous chondrites that belong to the CI,
101 CM, and CR classes contain abundant organic carbon that is present as a large variety of
102 organic molecules (e.g., Sephton 2002; Pizzarello et al. 2006; Schmitt-Kopplin et al. 2010),
103 whose precursors have, in several instances, been traced to pre-solar environments (e.g.,
104 Pizzarello and Huang 2005). These carbonaceous chondrites are also of intense interest
105 because similar materials are thought to be present on asteroid 101955 Bennu, which is the
106 focus of the current NASA lead OSIRIS-REx sample return mission (Lauretta et al. 2019),
107 and asteroid Ryugu, which was visited by the Hayabusa2 mission operated by the Japanese
108 space agency JAXA. Thus, the detailed study of the carbonaceous chondrites provides the
109 framework and basic knowledge with which to study the samples returned from Ryugu and
110 Bennu.

111   Particularly and intensely studied is the Murchison meteorite (e.g., Kvenvolden et
112 al. 1970; Fuchs et al. 1973; Schmitt-Kopplin et al. 2010), which fell near Murchison,
113 Australia, 28th September, 1969 (Fuchs et al. 1973). This meteorite provided the first
114 evidence for extraterrestrial chiral amino acids (Kvenvolden et al. 1970), and has become
115 the reference material for extraterrestrial organic chemistry. However, the long terrestrial
116 residence times of these and other CM2 falls, and their varied curatorial histories leads to
117 significant terrestrial contamination (Velbel and Palmer 2011). Since the fall of Murchison,
118 there have only been five collected CM2 falls – Sayama (1986), Maribo (2009),
119 Mukundpura (2017), Shidian (2017), and Aguas Zarcas (2019). Sayama, Maribo, and
120 Shidian are relatively small falls and little, if any, is available for study. In addition, both
121 Sayama and Maribo were intensely rained on before being collected. This rain will
122 significantly alter the soluble organic inventory and can also change the mineralogy
123 (Haberle and Garvie 2017). Mukundpura is also challenging to study as relatively little of
124 this single-stone fall is available to the scientific community. The recent abundant fall and

125   rapid recovery of the Aguas Zarcas CM2 chondrite (Garvie et al. 2019; Lücke et al. 2019),
126   provides the opportunity to study a pristine Murchison-like meteorite with short terrestrial
127   residence and little contamination.
128   In this study, I describe the bulk mineralogy from multiple stones from the Aguas
129   Zarcas fall. Most the mineralogical understanding comes from powder X-ray diffraction
130   (XRD) patterns acquired from ~1-mm-sized fragments chosen from a range of stones and
131   fragments, and their similarities and differences with other CM2 falls is explored. Only
132   pristine, pre-rain stones were used in this study.
133
134   **METEORITES STUDIED**
135   Approximately 100 Aguas Zarcas stones were collected prior to rains hitting the
136   fall site and provided to the Center for Meteorite Studies where they are stored under a dry
137   nitrogen atmosphere. These stones, comprising several kilograms of material, were
138   collected within three days of the fall. Pieces from thirteen separate stones and fragments
139   were studied, primarily by powder XRD (Table S1). Aguas Zarcas consists of individual
140   fusion-crusted stones (Fig. 1A) ranging from 0.1 g to 1868 g (Lücke et al. 2019). Most
141   stones are covered in fusion crust, but many broke upon impact with the ground. Stones
142   under ~50 g are typically angular to blocky and lack regmaglypts. Larger stones, especially
143   those near 1 kg, show broad regmaglypts, some well-developed (Lücke et al. 2019). Pre-
144   rain material crushed in a few milliliters of water emits a powerful "Murchison-like" odor,
145   though with a more prominent compost-like scent. While dry stones do not emit a
146   detectable odor, those exposed to rain were exceedingly pungent, so much so, that wet
147   stones could be located in the jungle around Aguas Zarcas by smell alone (M. Farmer, pers.
148   comm.). The crushed material in water tastes strongly of sweet Brussel sprouts.
149   In hand specimen, the interiors of the stones show a largely featureless dark gray to
150   black matrix studded with small (<1 mm) light-colored speckles (Fig. 1B). Petrographic
151   analysis show these speckles to consist of chondrules, sparse calcium aluminum-rich
152   inclusions (CAIs), and mineral fragments (Garvie et al. 2019; Kouvatsis and Cartwright
153   2020; Davidson et al. 2020). Larger, cm-sized broken surfaces show brecciation, which at
154   the cm-scale is dominated by two lithologies; chondrule-rich and -poor. These two
155   lithologies are recognized in hand specimens by their distinct ratio of inclusions +
156   chondrules to matrix. Chondrules + inclusions constitute ~10 to 15 areal% of the
157   chondrule-poor lithology and ~40 areal% in the chondrule-rich lithology. A third lithology,
158   here called the matrix-rich lithology, contains <1 areal% chondrules + inclusions, occurs
159   randomly as mm- to 1-cm-sized patches across the stones, and as a 4.3 g half stone
160   #2121_7. However, in hand samples, the three lithologies are intimately associated and the
161   boundaries between them are typically visually indistinct. Many cm-sized fragments show
162   visual chondrule + inclusion amounts between the chondrule-rich and –poor areas, and
163   only rarely does a fractured surface show a visually distinct clast with a sharp boundary.
164   However, for the discussions here, representative fragments have been chosen that fall into

165 the three "visual" categories of chondrule-rich, chondrule-poor, and matrix-rich. A fourth
166 macroscopic lithology is recognized in polished sections as it is relatively rich in Fe-Ni
167 metal and is chondrule poor. The metal-rich lithology is relatively uncommon and most of
168 the results and discussion below are for the three dominant lithologies.
169
170   **METHODS**
171   Powder XRD patterns were acquired from 13 stones and fragments with a Rigaku
172 MiniFlex 600 diffractometer (Table S1). This diffractometer is operated with Cu $K\alpha$
173 radiation and is equipped with a post-diffraction graphite monochromator and automatic
174 divergence slit system. Data were acquired from 2° to 65° 2θ at 0.02° steps, and 30 to 60
175 s/step. XRD samples were prepared from an ~1- to 2-mm-sized fragment, which weighs
176 ~10 mg. The chips were crushed and lightly ground to a fine powder and mixed with a few
177 milliliters of dry methanol. The resulting slurry was pipetted and spread into a thin, smooth
178 film on a low-background, single-crystal, quartz plate. This slurry was dried rapidly (~5 s)
179 under flowing warm air forming a thin film. Selected prepared XRD slides were subjected
180 to standard clay mineral treatments (Moore and Reynolds 1989) prior to X-ray data
181 acquisition, viz., ethylene glycol vapor at 60° C for 24 hr, heating to 300° C under an Ar
182 atmosphere for 1 hr, and after heating to 500° C under an Ar atmosphere for 1hr.
183   Thermogravimetric (TG) data was acquired under flowing He from 20° to 1000°
184 C, with a heating rate of 10° C/min. Data were acquired from a chondrule-rich fragment
185 (from stone #2121_8), chondrule-poor fragment (from stone #2121_5), matrix-rich
186 lithology (from stone #2121_7), and for comparison, a fragment of Murchison. Starting
187 masses for the Aguas Zarcas samples were as follows: #2121_8, 20.01 mg; #2121_5, 19.76
188 mg; and, #2121_7, 19.76 mg. Evolved Gas Analysis (EGA) was undertaken on ~40 mg of
189 powder prepared from a powdered 3 g piece of a representative piece of #2121_5. The
190 sample was loaded and evacuated to millitorr range and then heated to 1000° C under
191 dynamic pumping, with a heating rate of 4 °C/min. EGA data were recorded with a
192 Stanford Research Systems RGA 200, scan speed 3, mass/charge ratios 1-100 collected in
193 continuous sweeps. TG and EGA were undertaken in the Eyring Materials Center at
194 Arizona State University.
195   Soluble salts were extracted from fragments of meteorite by immersion in 5 ml of
196 RO water and warmed to 50° C for 10 minutes. The water was poured off and another 5
197 ml added. This processes was repeated five times and the 25 ml of water was then
198 evaporated to dryness leaving a hard creamy yellow, crystalline residue. As a test, 25 ml
199 of the RO water was evaporated to dryness and no residue formed.
200   Three typical fragments from stones #2121_5, #2121_7, and #2121_8 were
201 mounted in epoxy and polished. These samples were analyzed at the University of
202 Arizona's Michael J. Drake Electron Microprobe lab with a CAMECA SX100 electron
203 microprobe. Backscattered electron (BSE) imaging, energy dispersive spectroscopy

204 (EDS), and wavelength dispersive spectroscopy (WDS) analyses were used to determine
205 the elemental compositions of the samples.
206
207

RESULTS AND DISCUSSION

Powder X-ray diffraction

210   Powder XRD patterns from 25 separate ~1-mm-sized chips from the 13 stones and
211 fragments are all dominated by reflections from serpentine group minerals, on which are
212 superimposed reflections for ferrotochilinite, 1:1 interstratified
213 ferrotochilinite/cronstedtite, anhydrous silicates, calcite, Fe-Ni sulfides, and minor phases
214 (Fig. 2). Reflections for calcite are present in all samples. Stones with visible chondrules
215 show prominent reflections for forsterite and lesser enstatite. Pentlandite and pyrrhotite
216 reflections, which are of low intensity, are present in all samples studied. Reflections for
217 magnetite are only visible in the metal-rich clast (see discussion below).
218   There are two serpentine pattern types based on the intensities and d-spacings of
219 their reflections in the 32° to 46° 2θ (Cu Kα) range, as exemplified by the chondrule-poor
220 fragments (Fig. 2A and B) and a 5-mm clast composed of the matrix-rich lithology (Fig.
221 2C). In addition, the pattern type shown in Fig. 2C shows a distinct low-angle scattering to
222 the serpentine basal reflection centered near 8.6 Å (indicated as a "?" in Fig. 2C). The
223 profiles from the chondrule-rich fragments (not shown) are similar in shape to those from
224 the chondrule-poor fragments, expect with higher intensity reflections for the anhydrous
225 silicates. A third pattern type is from the metal-rich lithology (Fig. 2D). The overall
226 character of the serpentine reflections, i.e., shape, d-spacing, and intensities, from the
227 chondrule-poor and -rich lithologies are similar in shape to each other. Further discussions
228 on the identity of the serpentines, interstratified ferrotochilinite/cronstedtite,
229 ferrotochilinite, and the 8.6 Å reflection are provided below. The character of the high d-
230 spacing (low 2θ) range of the XRD patterns displayed on a log-scale after background
231 subtraction (Fig. 3), more clearly reveals the weaker reflections above 7 Å. The origins of
232 these reflections are described below. The diffraction pattern from the metal-rich lithology,
233 which is a relatively clast poor, differs significantly from the other patterns, and so is
234 discussed separately below.
235

236 **Identity of the serpentines**: The sharp and intense reflection present in all samples with a
237 d-spacing of 7.237 to 7.259 Å is consistent with the basal spacing of serpentine (Brindley
238 and Brown, 1984). This basal reflection does not show splitting or measurable unresolved
239 maxima (Fig. 3, peak #4). The XRD patterns up to ~32° 2θ (~2.8Å) exhibit two sharp 00*l*
240 reflections, and a well-defined 02-prism characteristic of disordered 1:1 phyllosilicate
241 stacking (Brindley 1984). Despite this disorder, both pattern types show distinct serpentine
242 reflections above ~32° 2θ (Table 1) that give insights into the bulk clay mineralogy. The
243 XRD powder patterns from many of the chondrule-poor and –rich fragments are

244 remarkably similar in shape to the pattern from Murchison (Fig. 2A and M). In particular,
245 the positions and d-spacings of the serpentine reflections closely match each other,
246 suggesting that the serpentine diversity in both is similar.
247   Early studies, e.g., Fuchs et al. (1973), interpreted the serpentine reflections from
248 Murchison as arising from monoclinic and hexagonal berthierine (referred to as
249 "chamosite" in their publication, though this name is now used for Fe-rich members of the
250 chlorite group). However, the d-spacings for berthierine (Brindley 1951), including the
251 ferrous variety (Brindley and Youell 1953), do not match the more intense d-spacing below
252 ~2.7 Å. For example, Fuchs et al. (1973) interpreted their 2.70, 2.44, and 2.16 Å reflections
253 from Murchison as matching the 2.67, 2.40, and 2.15 Å reflections of the "chamosites"
254 from Carroll (1970): they interpret the shifts in d-spacings as arising from compositional
255 differences. They further state that their trio of d-spacings do not match those from
256 ferroantigorite at 2.72, 2.43, and 2.17 Å. However, the measured d-spacings from
257 Murchison show a closer match to ferroantigorite than to "chamosite". Further
258 interpretation requires an understanding of the expected reflections for specific groups of
259 polytypes.
260   From crystallographic considerations, Bailey (1969) identified four groups of
261 trioctahedral 1:1 layer polytypes based on the presence or absence of strong and weak
262 reflections, viz., Group A ($1M$-$2M_1$-$3T$), Group B ($2Or$-$2M_2$-$6H$), Group C ($1T$-$2T$-$3R$),
263 and Group D ($2H_1$-$2H_2$-$6R$). The characteristic d-spacings from Bailey (1969) that allow
264 the different polytype groups and polytypes to be distinguished are calculated for
265 $Mg_3Si_2O_5(OH)_4$. However, numerous studies (reviewed in Brearley and Jones 1998) show
266 that many of the serpentines in CM chondrites are Fe-rich, many with compositions that
267 match cronstedtite (e.g., Bunch and Chang 1980; Zega and Buseck 2003; Pignatelli et al.
268 2018), though there is a wide range of compositions (Zolensky et al. 1993; Zega et al.
269 2006). Eight cronstedtite polytypes have been recognized from terrestrial samples, viz.,
270 $1M$, $2M_1$ and $3T$ (Group A); $1T$ and $2T$ (Group C); and $2H_1$, $2H_2$ and $6R$ (Group D).
271 Cronstedtite forms relatively large well-crystallized grains in many CM2 chondrites, and
272 as such have been extensively studied by TEM, electron diffraction, and electron energy-
273 loss spectroscopy (Zega and Buseck 2003; Zega et al. 2003; Pignatelli et al. 2018). For
274 example, cronstedtite from the Paris CM2 chondrite is dominated by the $1T$ polytype, with
275 one crystal having recognizable $3T$ and $2M_1$ polytypes (Pignatelli et al. 2018). The detailed
276 study of Pignatelli et al. shows that many of the grains belong to Bailey's Group C, but
277 further identification of the specific polytype is hampered by the abundant stacking
278 disorder.
279   The powder XRD patterns from the Aguas Zarcas serpentine shows two end-
280 member patterns as exemplified by the chondrule-poor fragment in Fig. 2A and the matrix-
281 lithology in Fig 2C. As shown by Bailey (1969), the serpentine polytypes show
282 characteristic reflections below ~2.8 Å (above ~32° 2θ) and these patterns differ
283 significantly in this 2θ range (Fig. 4). The profile from the chondrule-poor fragment (Fig.

284 4A) best matches the pattern from 1T cronstedtite (Hybler 2006), which belongs to Bailey
285 polytype group C (Bailey 1969), with lesser 1M cronstedtite (Table 1). In the experimental
286 pattern, the 110 reflection is split into two peaks suggesting the presence of two polytypes
287 or two distinct mineral species. In addition, the 112 and 113 reflections are broad,
288 consistent with a range of compositions and/or fine-grained sizes. The pattern from the
289 matrix-lithology (Fig. 4B) matches that of 1M cronstedtite (Hybler 2014) of Bailey
290 polytype group A. The -132 and 132 reflections (Fig. 4B) show an unresolved high-angle
291 reflection suggesting two distinct serpentine compositions of the 1M polytype. A peak near
292 2.55 Å and weak reflection near 2.17 Å suggest a minor amount of the 1T polytype. Further
293 identification of the specific polytypes is not possible because the experimental data is
294 broad, and distinguishing between 1M and 3T of the Bailey group A is based primarily on
295 weak reflections, which are not present in the experimental patterns. No evidence was
296 found for reflections for polytypes from Bailey Group D. For example, the $2H_1$ and $2H_2$
297 polytypes both show a significant reflection near 1.97 Å (Bailey 1988a), which is absent
298 in the patterns in Fig. 4. No cronstedtite polytypes are found that belong to Bailey Group
299 B and comparison with the spacings based on $Mg_3Si_2O_5(OH)_4$ (Bailey 1969) is problematic
300 as there are significant d-spacing shifts between the Mg-endmember and cronstedtite.

301   Serpentine is the most abundant mineral in CM1, CM1/2, and CM2 chondrites (e.g.,
302 Howard et al. 2009; Garvie et al. 2020), yet identification of specific mineral species by
303 powder XRD is hampered by their fine-grained nature, variable compositions, stacking
304 disorder, and co-occurrence of several mineral species within the same sample. For
305 example, using X-ray diffraction, Bunch and Chang (1980) identified at least four
306 phyllosilicates [*sensu stricto* serpentines] in Murray. In combination with SEM-EDX, they
307 further showed wide compositional ranges, but possible groupings of mineral species based
308 on composition, density, and color. Transmission electron microscopy further illustrates
309 the serpentine compositional, structural, and morphological variability (McKee and Moore
310 1979; Barber 1981; Zega and Buseck 2003; Zega et al. 2006). The good match between
311 the patterns for 1M and 1T cronstedtite and the Aguas Zarcas patterns (Fig. 4), especially
312 in the 30° to 55° 2θ region, suggests that the meteorite contains a significant component of
313 Fe-rich clays, some with compositions that overlap with those of cronstedtite. While this
314 match allowed for the primary Bailey polytype groups to be discerned, the deviations of
315 the d-spacings between the calculated and Aguas Zarcas patterns suggests that as a bulk,
316 the Aguas Zarcas clays are not cronstedtite, consistent with previous studies (e.g., Bunch
317 and Chang 1980).

318   The differences between the structurally characterized, primarily terrestrial,
319 serpentines and those in Aguas Zarcas are illustrated by plotting their d-spacings within
320 the "060" region of the XRD patterns (Fig. 5, Table 2). This X-ray region, centered around
321 60° 2θ, is used to distinguish between dioctahedral and trioctahedral serpentines (Wilson
322 1987), with spacings around 1.49 Å and 1.55 Å, respectively. This 2θ region from Aguas
323 Zarcas is similar in most patterns, excluding the metal-rich lithology (Fig. 2D), and best

324 illustrated by the pattern from the matrix-rich lithology (Fig. 5A). This pattern shows
325 maxima at 1.575 Å and 1.543 Å, and shoulders near 1.586 Å, 1.554 Å, and 1.524 Å. The
326 X-ray patterns from other fragments are similar (Fig. 5B and C). Plotting the reflections
327 from end-member 1M and 1T cronstedtite shows that its most intense reflection(s) in this
328 region overlaps with the low-angle shoulder to the 1.586 Å reflection, consistent with the
329 presence of this mineral. However, the relatively low intensity of the reflection that gives
330 rise to the 1.586 Å shoulder suggests that cronstedtite *sensu stricto* is a relatively minor
331 component of the bulk serpentine inventory. A similar conclusion was reached by Bunch
332 and Chang (1980) from the Murray CM2 chondrite. Greenalite, an Fe^{2+}-rich serpentine,
333 has a reflection that matches the 1.575 Å reflection, though the absence of an
334 accompanying intense reflection at 1.614 Å (Table 2) suggests that chemically and
335 structurally similar serpentines are not dominant. Similarly, overlapping the primary
336 reflections from a range of terrestrial Mg- and Fe-rich serpentines shows that the Fe-rich
337 serpentines odinite and berthierine overlap with the shoulder at 1.554 Å, and amesite and
338 chrysotile with the shoulder near 1.524 Å. None of the structurally characterized
339 serpentines have reflections that overlap with the maxima at 1.575 Å and 1.543 Å. If each
340 of the Aguas Zarcas maxima and their shoulders in the "060" region reflects structurally
341 and chemically distinct serpentine, then this meteorite contains at least four chemically and
342 structurally distinct serpentines.

343   The Aguas Zarcas XRD patterns show considerable bulk mineralogical diversity as
344 revealed by the variable intensities of the ferrotochilinite and regularly interstratified
345 ferrotochilinite/cronstedtite reflections between different samples. In addition, different
346 fragments range from those dominated by 1T cronstedtite to those dominated by 1M
347 cronstedtite. Among the 25 samples X-rayed, there is a positive correlation between the
348 intensity of the reflections for the cronstedtite 1M polytype and the intensity of the broad
349 8.6 Å reflection. In addition, the 1M-rich samples are poor in ferrotochilinite and regularly
350 interstratified ferrotochilinite/cronstedtite.

351   A question arises as to whether Aguas Zarcas as a CM2 is unique in showing such
352 mineralogical diversity. To address this question, four visually distinct 1-mm-sized
353 fragments of Murchison were X-rayed (Fig. S1). Each shows similar mineralogical and
354 polytype diversity as seen in Aguas Zarcas, though absent the broad 8.6 Å reflection.
355 Hence, much of the mm-scale mineralogical diversity measured in Aguas Zarcas is also
356 present in other CM2 chondrites (e.g., Lentfort et al. 2020). In addition, the level of
357 mineralogical diversity will to some extent also depend on the scale of the x-ray
358 measurements. At the micron scale, individual components can be probed. For example,
359 Nakamura and Nakamuta (1996) measured X-ray patterns from 50 μm-sized pieces of
360 Murchison. At this spatial scale, individual matrix components were sampled.

361

362 **Ferrotochilinite:** A 5.4 Å reflection corresponding to the 002 reflection (I_{obs} = 100) of
363 "tochilinite" is present from many, but not all the Aguas Zarcas samples studied. This

364   mineral was particularly abundant in a chondrule-poor clast from stone #2121_6 (Fig. 2B
365   and 3E). This reflection is typically the only one visible for this mineral from the CM2
366   carbonaceous chondrites, and only rarely are other reflections visible, e.g., the 10.8 Å 001
367   reflection (Fig. 3E and Murchison Fig. S2). Other reflections are rarely visible because
368   their intensities are weak (Nakamura and Nakamuta 1996; Pekov et al. 2013), and they
369   overlap with the more dominant reflections from the other phases in the CM2 chondrites.

370   In addition to the intense 002 (I_{obs}=100) reflection, tochilinite, *sensu stricto*, as
371    $6FeS.5Mg(OH)_2$, shows relatively intense reflections at 10.64 Å (I_{obs}=30), 2.605 Å
372   (I_{obs}=30), and 1.835 Å (I_{obs}=50). The tochilinite structure consists of alternating layers of
373   brucite/amakinite-like $(Mg,Fe)(OH)_2$ and mackinawite-like $(Fe,Ni)_{1-x}S$ layers (Organova
374   et al. 1973, 1988). In comparison, ferrotochilinite, $6FeS.5Fe(OH)_2$, shows weak reflections
375   other than the 5.4 Å peak (Pekov et al. 2013), with the 10.83 Å reflection of I_{obs}=13.
376   Ferrotochilinite differs from tochilinite in containing dominantly Fe in the hydroxide layer
377   (Pekov et al. 2013). The low intensity of the 001 "tochilinite" reflection in comparison to
378   the 002 peak in the Aguas Zarcas and Murchison XRD profiles (Fig. 3E, S2), is indicative
379   of a high content of Fe in octahedral sites (e.g., Mackinnon and Zolenksy 1984), and thus
380   the meteoritic mineral is consistent with ferrotochilinite (Pekov et al. 2013).

381   The presence and absence of ferrotochilinite in the Aguas Zarcas implies a
382   relatively narrow temperature range for its formation and maximum temperature for post-
383   formational heating. The mean precipitation temperature for tochilinite is estimated at 120°
384   to 160° C for CM chondrites (Vacher et al. 2019), though a wider T range is dictated by
385   the S fugacity (Kozerenko et al. 2001). Differential scanning calorimetry (DSC) of
386   tochilinite shows dehydroxylation starting near 450° C (Gooding and Zolensky 1987).
387   However, the decomposition temperature of tochilinite depends strongly on experimental
388   heating conditions and the origin of the material. The experiments of Gooding and
389   Zolensky (1987) were conducted with terrestrial tochilinite heated under a steady flow of
390   dry N_2. Whereas, Fuchs et al. (1973) heated samples of Murchison in vacuo at 245 ° C and
391   noted the disappearance of the 5.4 Å reflection from tochilinite. However, in my
392   experiments, the 5.4 Å reflection from the Aguas Zarcas tochilinite remained unchanged
393   after heating to 300 ° C under flowing He, but was not present after heating to 500 °C.
394   These data suggest a wide temperature range for the dehydroxylation of tochilinite, but
395   also suggests factors such as composition (tochilinite versus ferrotochilinite), crystallinity
396   and grain size, and experimental run conditions, e.g., in vacuo versus gas, affect the
397   decomposition temperature.
398
399   **Regularly interstratified ferrotochilinite/cronstedtite:** Many, but not all, of the
400   chondrule-poor and –rich stones show a weak- to medium-intensity reflection centered at
401   6.05 Å (Fig. 2A, 3B,C). This peak was identified as the 003 reflection from interstratified
402   ferrotochilinite/cronstedtite (Nakamura and Nakamuta 1996). Further confirmation for this

403   peak identification comes from the presence of small but discernible peaks at ~18.3 Å
404   (001), 9.09 Å (002), and 4.53 Å (004).

405   Mackinnon and Zolensky (1984) proposed that the ~17 Å reflection measured by
406   high-resolution transmission electron microscopy (HRTEM) arises from the
407   "commensurate intergrowth of serpentine and tochilinite layers". Further, Zolensky et al.
408   (1993) showed high-resolution TEM images of coherently interstratified tochilinite and
409   cronstedtite. The ~18.3 Å reflection measured from Aguas Zarcas (Fig. 3B, C) and
410   Murchison (Fig. 2M), is approximately equal to the sum of the thickness of the 7.2 Å basal
411   spacing from serpentine and 10.8 Å of ferrotochilinite (Fig. 6). Such an intergrowth gives
412   rise to a rational series of 00l reflections arising from the regular ordering of ferrotochilinite
413   (T) and cronstedtite (C), with equal proportions of T and C, where the probability of finding
414   a T followed by a C is 1.0 and vice versa. With this ordering, the diffracting domains are
415   built up of units such as …TCTCTCTC… This type of ordering is referred to as regular
416   1:1 interstratification (Bailey, 1981).

417   The relative intensities of the 00l reflections for regularly interstratified
418   ferrotochilinite/cronstedtite were calculated by Nakamura and Nakamuta (1996), showing
419   strong 003 and medium-intensity 004 reflections. Other reflections are of low intensity,
420   and except for the 001 and 002, are typically obscured by the more intense reflections from
421   the dominant minerals. Despite its low intensity, the 001 reflection is fortuitously visible
422   as there are no other reflections from meteoritic minerals in this 2θ region. Whereas
423   HRTEM images show a range of T/C stacking sequences in CM chondrites (Zolensky et
424   al. 1993), my diffraction data from Aguas Zarcas shows that regular 1:1 interstratification
425   arising from …TCTCTCTC… stacking is sufficiently abundant to give rise to distinct
426   reflections. Other sequences are likely present, but are not sufficiently abundant to give
427   rise to measurable reflections in the XRD patterns. A point of observation, fragments with
428   the most intense 6.05 Å reflection from regularly interstratified ferrotochilinite/cronstedtite
429   only show a low intensity 5.4 Å reflection for tochilinite, and *vice versa*, e.g., compare Fig.
430   2A and B.

431   The regularly 1:1 interstratified ferrotochilinite/cronstedtite, which gives a
432   fundamental basal spacing of 18.3 Å in the Aguas Zarcas and other CM2 meteorites (e.g.,
433   Nakamura and Nakamuta 1996), is an unnamed mineral. The IMA Commission on New
434   Minerals and Mineral Names allows for naming of regular interstratifications of two or
435   more minerals (Bailey 1981; Nickel and Grice 1998). Mineral names are given to regular
436   interstratifications where the kinds of layers, their relative proportions, elemental
437   compositions and regularity of interstratification is well documented (Bailey 1981). For
438   example, tosudite is the regular 1:1 interstratification of dioctahedral chlorite-smectite,
439   which gives rise to a fundamental basal spacing of 28.89 Å (Bailey 1981; Garvie 1992).
440   To merit a name, the interstratification should have sufficient regularity to give at least ten
441   00l summation spacings (Bailey 1981). In the case of the interstratified ferrotochilinite and
442   cronstedtite from Aguas Zarcas, the only reflections visible in the powder XRD patterns

443   are at 18.3 Å (001), 9.09 Å (002), 6.05 Å (003), and 4.53 Å (004) [Note: Nakamura and
444   Nakamuta (1996) also detected the 005 reflection near 3.63 Å from Murchison]. The
445   higher-order reflections above $l = 5$ are not visible from my bulk powder XRD patterns as
446   they have such low intensities (Table 1 in Nakamura and Nakamuta 1996), and they overlap
447   with the intense reflections from the dominant minerals. Despite these experimental
448   difficulties, the relatively common occurrence of the easily detectable reflection at 6.05 Å,
449   attributed to the 003 spacing for 1:1 regularly interstratified ferrotochilinite/cronstedtite,
450   shows this mineral to be relatively widespread in the CM2 chondrites. As such, further
451   characterization and naming of this mineral is warranted.
452
453   **The 8.6 Å peak:** Particularly noticeable from the powder XRD patterns from the matrix-
454   rich lithology, which include stone #2121_7, mm- to cm-sized fragments and areas of
455   stones #2121_11, 12, MF2, and a 5-mm rounded clast in #2121_5, is a distinct broad peak,
456   centered near 8.6 Å, on the low-angle side of the 7.2-Å-serpentine reflection (Fig. 2C, 3D).
457   This peak does not correspond to the 001 reflection of either 1:1 or 2:1 phyllosilicate
458   structures, or to known interstratified clays (Drits and Sakharov 1976; Brindley and Brown
459   1984). To gain a better understanding of this broad peak, the XRD slide was subjected to
460   "standard" clay treatments (Wilson 1987; Moore and Reynolds 1989).
461   The XRD pattern remains unchanged after heating to 300° C under an Ar
462   atmosphere (not shown), consistent with the stability of serpentine and tochilinite at this
463   temperature. In addition, the pattern remains unchanged after ethylene glycol treatment
464   (not shown), consistent with the absence of expandable layers. After heating to 500° C
465   under an Ar atmosphere for 1hr, the pattern changed dramatically, with the disappearance
466   of the broad 8.6 Å peak, reflections from serpentine, and tochilinite (Fig. S2). This heating
467   behavior of the Aguas Zarcas clays matches that for Murchison (e.g., Fuchs et al. 1973;
468   Morris et al. 2020). While the serpentine 00l reflections are absent, broad hk-band
469   scattering for phyllosilicates is still present, though of lower intensity compared with the
470   unheated pattern. The reflections between 20° and 40° 2θ (Cu Kα) sit on a low intensity
471   broad hump, centered around 30 °2θ, consistent with amorphous scattering. The heating
472   duration and peak temperature were not sufficient to form secondary olivine from the
473   dehydroxylated serpentine.
474   The broadness of the 8.6 Å peak indicates diffraction from a small crystallite size,
475   disorder, interstratification, or a combination thereof. This d-spacing does not correspond
476   to diffraction from either ideal 1:1 or 2:1 layered structures of the phyllosilicates, though
477   is close to the broad ~9.3 Å spacing for kerolite (Whitney and Eberl 1982), a fine-grained,
478   disordered, talc-like mineral often associated with serpentine. However, the absence of the
479   8.6 Å peak after heating to 500° C is incompatible with this mineral. Alternatively, this
480   broad reflection may correspond to randomly interstratified tochilinite-serpentine. These
481   intergrowth phases are common in CM chondrites (Fuchs et al. 1973; Brearley and Jones
482   1998; Vacher et al. 2019), but again, the 8.6 Å peak is not consistent with randomly

483   interstratified tochilinite-serpentine. At present, the origin of the broad 8.6 Å peak remains

484   obscure.

485

486   **Additional low-angle reflection:** Three of the fragments show a weak to medium-intensity

487   reflection near 14.7 Å. This reflection is most intense, though broad, in a chondrule-poor

488   clast from stone #2121_17 (Fig. 3A). This reflection is not consistent with serpentine,

489   whereas chlorite has a basal reflection near this d-spacing, though identification of minor

490   Fe-rich chlorite is hampered as its intense 7 Å reflection overlaps the basal reflection for

491   serpentine. Chlorite has been detected in CM chondrites (e.g., Zolensky et al. 1993), though

492   only as a minor constituent. However, the absence of an expected 003 reflection near 4.8

493   Å suggests that the 14.7 Å reflection does not arise from chlorite. The 14.7 Å reflection

494   remains unchanged after glycolation for 24 hours at 50°C, revealing the absence of

495   expandable layers. This peak may arise from the short-range association of layers that can

496   give rise to a single summation peak $d(001) = d_A + d_B$, where d_A and d_B are the fundamental

497   001 d-spacings of mineral A and B, respectively (Bailey 1981). Currently, the origin of the

498   14.7 Å is unknown.

499

500   **Metal-rich lithology:** The powder pattern from the metal-rich clast from stone #2121_16

501   shows a serpentine basal reflection at 7.255 Å, with an intense low-angle scattering starting

502   ~5° 2θ (Fig. 2D). The XRD pattern also shows medium- to low-intensity reflections for

503   forsterite, tochilinite, magnetite, pyrrhotite, pentlandite, kamacite, and dolomite. The

504   phyllosilicate reflections between 30° to 55° 2θ exhibit reflections more consistent with

505   the 1T cronstedtite polymorph rather than the 1M cronstedtite. However, the pattern in the

506   "060" X-ray diffraction region differs significantly from the other Aguas Zarcas patterns

507   (Fig. 5), and in particular, lacks the shoulder near 1.586 Å (region 2 in Fig. 5) attributed to

508   cronstedtite, and the maximum at 1.575 Å.

509   The low-angle scattering starting near ~5° 2θ and extending up to the low-angle

510   side of the 7.255 Å reflection is broader than the 8.6 Å peak described above and more

511   intense relative to the serpentine basal reflection than in the other patterns. In addition, the

512   low-angle scattering background below ~5° 2θ is considerably more intense compared with

513   the other diffraction patterns. This low-angle background arises from a range of effects

514   (van der Gaast and Vaars 1981), with the largest contributions from the Lorentz-

515   polarization factor, air scatter, small particles, and micropores. The XRD sample for the

516   metal-rich lithology was prepared and acquired in the same manner as the other samples,

517   suggesting that Lorentz-polarization factor and air scatter are not responsible for the higher

518   low-angle scattering intensity. Thus, the intense background below ~5° 2θ and the broad

519   scattering between ~5° and 12° 2θ suggests a significant proportion of small particles,

520   though there is no scattering contribution that would suggest a significant amorphous

521   component. Overall, the mineralogy of the metal-rich clast differs from the other clasts and

522   areas analyzed in Aguas Zarcas.

523
524 **Soluble salts**
525   A 3.3043 g fragment of stone #2121_6 extracted with water produced 21 mg of a
526 light-yellow crystalline residue, giving 0.6 wt% soluble salts. The initial dried extract is
527 crystalline (Fig. 7), but with a sticky consistency. It loses its stickiness when dried over
528 P_2O_5 for one week: its powder XRD pattern is dominated by a multitude of sharp reflections
529 (Fig. 8). Elementally appropriate matches against the inorganic section of the PDF database
530 include halite – NaCl; chlorartinite – $Mg_2(CO_3)(OH)Cl.2H_2O$; thenardite – Na_2SO_4; and
531 sodium chlorate – $NaClO_4$. Additional sharp reflections occur that cannot be matched to
532 phases in the Powder Diffraction File (PDF) database of the International Center for
533 Diffraction Data. The best match for chlorartinite intensities is achieved by modelling the
534 X-ray pattern from a partially hydrated phase, consistent with the dehydrating nature of the
535 P_2O_5. It is also possible that the dried extract contains water soluble organic species.
536 Formate and acetate were present at concentrations of 1.2 and 2.4 µmol/g, respectively in
537 the Aguas Zarcas water extracts (Pizzarello et al. 2020). A peak/match search against the
538 organic section of the PDF database produced several possible matches. However, these
539 matches are not discussed further in the absence of additional data, such as from infrared
540 spectroscopy.
541   It is unknown which of the minerals in the dried Aguas Zarcas water extract also
542 occur in the meteorite, as some may have formed during the drying and crystallization of
543 the extract. Calcite and fine-grained sulfides are abundant in the meteorite, and their partial
544 dissolution during the warm-water extraction would account for at least some of the
545 extracted HCO_3^-, sulfate, and Ca. Thenardite was found in the Murray (CM2) chondrite
546 (King and King 1981), suggesting that it also occurs in Aguas Zarcas and not formed solely
547 during the drying of the extracted solution. Some of the other highly soluble chlorides and
548 mixed cation and anion salts may also occur in Aguas Zarcas, but are at too low a
549 concentration to be detected by powder XRD.
550   Measuring the elemental composition of the water-soluble species in chondrites
551 provides data on the aqueous chemistry on their parent bodies. The composition of these
552 soluble species reflects the water/rock ratio, pH, and Eh of the aqueous environment
553 (Zolotov et al. 2018). As an aside, it is these soluble species that give rise to the evaporitic
554 weathering products, which include Mg carbonates and sulfates, on Antarctic meteorites
555 (Velbel 1988). Previous measurements of the nonvolatile water-soluble cations from
556 Aguas Zarcas show Na>Mg>K and the anions sulfate>chloride>acetate>formate
557 (Pizzarello et al. 2020). The minerals detected from my XRD analysis of the Aguas Zarcas
558 water extract contain Na, Mg, Ca, Cl, carbonate and sulfate, similar to those measured by
559 ion chomatrography (Pizzarello et al. 2020). The soluble species measured in Aguas Zarcas
560 match those from Murchison, which includes, at high concentrations, $HCO_3^- \approx SO_4^{2-} > Cl^-$
561 and $Na \approx Mg \approx Ca > K$ (Fanale et al. 2001, Zolotov et al. 2018). For Murchison, the
562 composition of water leachates could reflect that of chlorides, Mg/Na sulfates, putative Na

563   carbonates, and at least some Ca carbonates and sulfates (Zolotov et al. 2018). The high-
564   solubility chlorides, Na sulfates, and Mg carbonates could characterize late brines, and
565   sulfates reflect the action of strong oxidants in the parent body (Zolotov et al. 2018).
566
567   **Thermal gravimetric and evolved gas analysis**
568   A chondrule-rich fragment (from stone #2121_8), chondrule-poor fragment (from
569   stone #2121_5), and matrix-rich lithology (from stone #2121_7), show total mass losses
570   up to 1000 °C of 11.4, 13.5, and 14.7%, respectively (Fig. 9, Table 3). Following Garenne
571   et al. (2014), the TG loss curves can be divided into the following temperature regimes: **a)**
572   Room temperature to 200° C - desorption of H_2O and other volatile species; **b)** 200° to
573   400° C - release of H_2O from (oxy)-hydroxides; **c)** 400° to 770° C - dehydroxylation of
574   phyllosilicates; and, **d)** 770° to 900° C - decomposition of calcite and sulfates. Organic
575   matter is expected to oxidize in the 400° to 650° C range (Smykatz-Kloss 1974), though in
576   reality, the organic material from Murchison degrades over a wide temperature range from
577   250° to 1050° C (Kerridge et al. 1987).
578   The total mass losses for the three Aguas Zarcas stones parallels the visual
579   concentration of anhydrous silicates dominated by the chondrules and CAIs. The matrix
580   lithology stone (#2121_7) has the highest mass loss on par with that from Murchison (Table
581   3). These losses are within the range of other CM chondrites, such as the Antarctic CM
582   finds LEW 85312, LEW 90500, and heated CM chondrites (Garenne et al. 2014). Overall,
583   the lower mass losses for the Aguas Zarcas stones compared with Murchison could imply
584   a higher abundance of anhydrous phases, such as olivine and enstatite, which are common
585   in chondrules. While stone #2121_8 is chondrule rich, #2121_5 is matrix rich with few
586   chondrules. Another possibility for the lower mass losses is from an anhydrous amorphous
587   component, though there is little evidence for significant amorphous material in the
588   diffraction patterns.
589   The total low-temperature mass loss, up to 200° C, will to some extent depend on
590   the humidity of the air under which the sample is equilibrated, as well as the length of time
591   the sample is purged by H_2 in the TG apparatus. For example, a 5.2465 g fragment of stone
592   #2121_5, equilibrated under laboratory conditions with a relative humidity of ~30%, lost
593   ~1.7 wt% of mass when stored over P_2O_5 (Fig. 10). This mass loss is consistent with that
594   measured by TG up to 200° C. The sample shows an initial rapid mass loss during the first
595   24 hours, and then more gradual loss over the following weeks. This rapid-then-slow mass
596   loss may reflect loss and absorption of adsorbed and then mesopore water, respectively
597   (Garenne et al. 2014). The P_2O_5-induced mass loss is rapidly regained when the sample is
598   placed back into the air, and is an indication of the level of atmospheric contamination
599   experienced by these porous, clay-rich chondrites when they enter the Earth's atmosphere,
600   and subsequently exchange and equilibrate with atmospheric water vapor. This
601   atmospheric moisture can have significant effects on the measured H budget of

602 carbonaceous chondrites (Vacher et al. 2020), and demonstrates the importance of
603 appropriate curation of extraterrestrial samples.

604   Within the 200° to 400° C range, losses are between 2.3 and 3.3 wt% (Table 3);
605 these values overlap with a range of CM chondrites (Garenne et al. 2014). While the mass
606 loss in this region is attributed to release of H_2O from (oxy)-hydroxides, such phases were
607 not identified in the powder XRD patterns. Another possibility is mass loss from
608 ferrotochilinite. Published results on the stability and decomposition temperature of
609 tochilinite show a relatively wide temperature range. Terrestrial tochilinite decomposes
610 starting near 450° C (Gooding and Zolensky 1987). However, heating experiments on
611 Murchison show that the ferrotochilinite reflection at 5.4 Å loses intensity between 300°
612 and 400° C (Morris et al. 2020). The previous heating experiments were done on time-
613 scales of a few hours. Longer heating experiments (Fuchs et al. 1973), show the persistence
614 of the 5.4 Å reflection after heating to 245° C for 3.7 days, but is not present after continued
615 heating at this temperature for 7.7 days. It is also possible that some of the organic matter,
616 which typically oxidizes above 400° C, can also degrade at lower temperatures, possibly
617 initiated by the catalytic degradation by surrounding minerals (e.g., Kebukawa et al. 2010).
618 Further evidence for organic matter release is provided by the evolved gas analysis
619 experiment described below.

620   The greatest mass loss occurs in the 400° to 770° C range (Table 3), consistent with
621 the high serpentine content, as revealed by the XRD data. The H_2O content of serpentine
622 ranges from around 10 to 14 wt%, depending on the species (Newman and Brown 1987).
623 Thus, most of the high-temperature H_2O^+ loss is from the serpentine dehydration and
624 dehydroxylation, with lesser amounts from the organic compounds. The relatively small
625 mass loss in the 770° to 900 °C range is primarily attributed to calcite decomposition.

626   Assigning mass losses within defined temperature ranges to specific constituents
627 and minerals is complicated by several factors. Firstly, specific mass-loss regions are
628 typically defined for pure minerals, and the assumption is then made that the similar
629 minerals in meteorites chemically and structurally match that of the pure mineral standards,
630 and thus behave similarly with respect to heating. However, as indicated by the powder
631 XRD analysis above, the bulk clay minerals differ both elementally, and likely structurally,
632 from terrestrial serpentines. In addition, their fine-grained nature will also affect their
633 dehydroxylation temperatures. Thus, the relatively low onset temperature for the
634 dehydroxylation of the Aguas Zarcas serpentines, assigned to the rapid mass-loss onset
635 starting around 400° C, is significantly lower than for pure chrysotile, starting near 760°
636 C, which lowers to 600° C for Fe-rich varieties (Smykatz-Kloss 1974). Another factor that
637 could alter the expected measured decomposition temperatures arises from reactions within
638 a multimineralic system as minerals decompose and produce reactive gasses. For example,
639 dehydration and dehydroxylation of clays releases a suite of volatiles, including HF, H_2S,
640 SiH_4, NH_3, NO, HN_3, PH_3, and HCN, some of which decompose calcite (Heller-Kallai et
641 al. 1987, 1988; Heller-Kallai 1997). Given the potential reactivity of some of these species

642 (Heller-Kallai et al. 1988), it is likely that similar reactive species produced during the
643 Aguas Zarcas decomposition could alter the decomposition temperatures of the minerals
644 compared with reference mineral data.
645   Further insight into the mineralogical decompositions with respect to temperature
646 is provided from the Evolved Gas Analysis (EGA) data (Note: EGA is also referred to in
647 the literature as Residual Gas Analysis - RGA). This technique continuously measures the
648 partial pressures of evolved gases and volatiles released from a sample and measures their
649 mass-to-charge ratio (m/z) as a function of temperature. This method has been applied to
650 meteorites (Gibson and Johnson 1972, Morris et al. 2005; ten Kate et al. 2009; Verchovsky
651 et al. 2020). During heating, the sample decomposes and releases a multitude of primary
652 and secondary gaseous products (Fig. 11). The relative intensities of the peaks are semi-
653 quantitatively related to their concentrations (Gibson and Johnson 1972).
654   The most abundant gas released below 550° C has an m/z of 18, corresponding to
655 H_2O (Fig. 11A). Water vapor shows maximum release temperatures of 78°, 380°, and 480°
656 C. The first loss corresponds to water desorption, consistent with the low temperature TG
657 mass loss, consistent with that observed through drying over P_2O_5. The shape of the water
658 peak indicates that all absorbed water has been released by 150° C. The two higher
659 temperature losses peak at 373° and 470° C, with continued H_2O release up to ~700° C.
660 The overall H_2O release shape broadly overlaps the EGA profile from Murchison (Morris
661 et al. 2005). Likewise, the differential thermal gravimetric (DTG) profiles from a range of
662 CM chondrites all show two endothermic peaks in the 350° to 600° C region (Garenne et
663 al. 2014), attributed to dehydroxylation of Fe-Mg serpentines. The maximum gas release,
664 attributed primarily to H_2O, for a range of Fe-Mg serpentines, occurs over a wide
665 temperature range (Morris et al. 2005), peaking at 416° C for cronstedtite to 748° C for
666 antigorite. Thus, the lower dehydroxylation temperatures of the CM serpentines compared
667 with terrestrial analogues, reflects the fact that the meteoritic clays are fine grained,
668 structurally disordered, and Fe-rich.
669   A gas with m/z of 44, corresponding to CO_2, is approximately an order of
670 magnitude less intense than the H_2O profile up to 450° C, and then steadily rises in intensity
671 with two major gas releases at 605° and 663° C (Fig. 11A). The CO_2 evolved in the 300°
672 to 450° C region likely reflects decomposition and oxidation of organic matter, and this
673 explanation is further corroborated by the matching pattern for H_2 (not shown). The two
674 significant CO_2 releases are likely from carbonate decomposition, though the presence of
675 two rather than one peak suggests more than one mineral species, though the only carbonate
676 reflections identified are from calcite. The peak near 680° C corresponds to the maximum
677 CO_2 release during decomposition from calcite during slow heating rate of 6°/min
678 (Verchovsky et al. 2020), close to the rate of 4°/min used here. While the CO_2 release at
679 605° C is lower than measured for pure calcite (Verchovsky et al. 2020), a similar
680 maximum CO_2 release was measured from Murchison (ten Kate et al. 2009). To some
681 extent, the maximum release of CO_2 from calcite depends on the heating rate of the

682   experiment (Verchovsky et al. 2020). It is also possible, that the release of other volatiles
683   (Heller-Kallai et al. 1987, 1988; Heller-Kallai 1997) can affect the calcite decomposition
684   temperature and hence temperature of maximum CO_2 release.
685   Masses matching S-bearing gases were released at relatively low temperatures (Fig.
686   11B). Gases with m/z of 64, matching the masses of SO_2 and S_2, show maxima at 296° and
687   490° C, and H_2S with mass 34, have maxima at 392° and 481° C. Similar SO_2 release
688   temperatures were also measured from Murchison (ten Kate et al. 2010). Organic
689   compounds are difficult to recognize in the mass spectra, likely because of the complexity
690   of their decomposition and multiple low-mass interferences. However, a mass of 30, which
691   matches the molecular weight of formaldehyde and ethane, shows an increase in intensity
692   above 150° C and maximum at 376° C. This mass loss may correspond to the pyrolysis of
693   organic matter. A similar range of organic compounds were also identified by EGA from
694   Murchison (ten Kate et al. 2010).
695   The data presented here for Aguas Zarcas, show, as expected, significant release of
696   CO_2 and H_2O from the decomposition of phyllosilicates, organic matter, and carbonates.
697   The data also show the relatively low temperature, ~250° to 550° C, release of a range of
698   S-rich and organic gases (Fig. 11). In addition to the gases described above, heated
699   meteorites also release a range of labile elements, including S, As, Se, Te, Cd, Sb, and Hg
700   (Springmann et al. 2019). Many of the labile-element release patterns match the
701   temperature maxima for selected gases from Aguas Zarcas. For example, Hg is released
702   from a range of CM2 chondrites with a maximum near 280° C: a similar correlation is
703   shown for S. The water collected from the decomposition of Murchison was shown to
704   contain 7.9 mg/L of Hg (Kelsey and Lauretta 2013). The maximum Hg release temperature
705   is near the same temperature maximum measured for gases with an m/z of 64,
706   corresponding to SO_2 and S_2 from Aguas Zarcas, further suggesting an association between
707   Hg and S in the CM2 meteorites. Determining the abundance, type, and temperature
708   distribution of volatiles released during heating and subsequent thermal decomposition of
709   clay-rich extraterrestrial materials is important to future space missions designed to
710   incorporate in situ water extraction from water-rich asteroids. Extracted water can be used
711   for human consumption and rocket propellant. However, my and published data (e.g.,
712   Springmann et al. 2019), show that this water can be significantly contaminated, and even
713   exceed EPA limits for contaminants in drinking water (Kelsey and Lauretta 2013). Thus,
714   future space missions with an ISRU water-extraction component will require technologies
715   for water purification for human consumption.
716
717   **Correlating mineralogy with petrography**
718   Aguas Zarcas is visually a breccia, though only rarely are distinct clasts seen in
719   hand specimen that show a sharp boundary with the surrounding matrix. Most cut and
720   polished fragments show mm- to cm-scale variations from chondrule-rich to -poor.
721   Polished microprobe mounts were made from the three fragments of stones that are

722 chondrule-poor (#2121_5), matrix-rich (#2121_7), and metal-rich (#2121_8) (Figs. 12,
723 S3,4,5). These stones were also studied by powder XRD (Fig. 2). High-spatial-resolution
724 SEM images of these three visually distinct lithologies reveal markedly different matrix
725 petrographies (Fig. 12). In general, many of the petrographic features observed for the
726 Aguas Zarcas sections overlap with those from Murchison and Murray (e.g., Fuchs et al.
727 1973, Bunch and Chang 1980; Nakamura and Nakamuta 1996; Brearley and Jones 1998),
728 and the focus here will be on distinctive matrix features.

729   Low-magnification BSE images of the chondrule-poor stone (#2121_5, Fig. S3)
730 show scattered chondrules, many with thick fine-grained dust rims, and rounded fine-
731 grained clasts (indicated as fgmc in Fig. 12A and S3), supported by a matrix with prominent
732 ~50 to 150 μm rounded and sub-rounded Fe-S-rich objects. These sub-rounded objects are
733 morphologically similar to the tochilinite-cronstedtite-intergrowths TCIs (formerly called
734 "poorly characterized phases" PCP) from CM chondrites (e.g., Bunch and Chang 1980;
735 Nakamura and Nakamuta 1996; Brearley and Jones 1998; Lentfort et al. 2020), specifically
736 the "fibrous needle clusters (type II)" TCI objects (Bunch and Chang 1980; Nakamura and
737 Nakamuta 1996). Particularly noticeable is the common occurrence of embayed, anhedral
738 grains of calcite in the TCI objects (e.g., Fig. 12A), previously noted from Murchison
739 (Bunch and Chang 1980; Brearley and Jones 1998). High-resolution SEM images show
740 that these TCI objects typically have an internal bladed morphology (Fig. 12A and B), with
741 low-Z dark material between the blades. Individual blades are up to 2 μm wide and 15 μm
742 long. WDS analyses of the bladed grains show high Fe and S, consistent with
743 ferrotochilinite, and wt% levels of Mg and Si (Table 4). The presence of Mg and Si in these
744 blades may indicate interstratification with serpentine, or X-ray signal from the
745 surrounding serpentine. The darker material between the blades is similarly difficult to
746 analyze because it is typically only a few microns-across. One dark 4-μm-wide area
747 between the bright blades has Fe/(Fe+Mg) (in wt%) of 0.4, which is lower than most
748 Murchison clay analyses, though within the serpentine field for Nogoya, Cold Bokkeveld,
749 and ALH 88045 (Zolensky et al. 1993). Powder XRD patterns from similar regions shown
750 in the SEM image in figure 12A are dominated by serpentine, with variable amounts of
751 ferrotochilinite and 1:1 regularly interstratified ferrotochilinite/cronstedtite (Fig. 2A and
752 B). The calcite present in the BSE images is also prominent in the XRD patterns. Pyrrhotite
753 and pentlandite are identified by powder XRD, but only as a minor constituent. These
754 minerals occur scattered across the section as sparse <50-μm-sized grains.

755   A typical BSE image of the matrix-rich lithology shows rare dispersed chondrules
756 and mineral fragments set in a fine-grained matrix (Fig. S4). At higher magnifications, the
757 BSE images show intimately interspersed, but texturally separated, three-phase mixture,
758 viz., darker materials with scattered bright grains (M1 in Fig. 12C); medium-bright with
759 speckled appearance (M2 in Fig. 12C); and, bright, sinuous but connected network that
760 locally surrounds a low-Z material (arrowed material in Fig. 12C). WDS data from the
761 three matrix materials show low totals (Table 4), consistent with their hydrated nature. In

762   addition, their brightness in the BSE images correlates with their Fe content. The SEM-
763   based microprobe analysis does not have the necessary spatial resolution to provide
764   elemental data on the individual micron and sub-micron-sized components that make up
765   the matrix materials. However, WDS data from the dark material (M1) shows a relatively
766   narrow compositional range (Table 4), with Fe/(Fe+Mg) (in wt%) of 0.3, which is lower
767   than the serpentine data for Murchison, but overlaps the low end of the serpentine analyses
768   from ALH 88045 and Nogoya (Zolensky et al. 1993). The low S content likely derives
769   from minor sub-micron-sized, unresolved, sulfides with the clay. However, the S may also
770   be structurally associated with the serpentine (Zega et al. 2004). Characteristic of the XRD
771   patterns from the matrix-rich lithology is the prominent 8.6 Å reflection. However, the
772   absence of correlated micron-scale diffraction and WDS analyses prevents the
773   identification of this material in the BSE images.
774   Low-resolution BSE images of the metal-rich lithology (Fig. S5) show chondrules
775   (type I and II), silicate fragments, metals, and sulfides supported by a fine-grained matrix.
776   At this low magnification, the matrix appears relatively uniform in comparison with the
777   TCI-rich matrix (Fig. S3). At higher magnifications (Fig. 12D), the BSE images reveal
778   matrix composed of darker clasts (typically <20 μm diameter) bordered by thin (~1 μm)
779   bright rims, and interspersed with regions exhibiting a speckled texture (M2 in Fig. 12D).
780   At the resolution of the SEM, the contrast is uniform across many of the darker clasts,
781   which lack bright, high-Z grains. WDS data from the dark clasts are Mg- and Fe-rich, with
782   Fe/(Fe+Mg) (in wt%) of 0.6, similar to the average serpentine composition from Murchison
783   (Zolensky et al. 1993). The rims contain more Fe and less Mg than the dark cores, but also
784   lower S (Table 4). The low S content suggests that tochilinite is not a major component of
785   the bright materials in the BSE images, consistent with the relatively low-intensity of the
786   5.4 Å reflection in the XRD pattern (Fig. 2D). Also, cronstedtite is not likely a major
787   component as the "060" of the XRD pattern lacks the characteristic reflection for
788   cronstedtite near 1.58 Å. Hence, the identity of the bright rims around the low-Z, darker,
789   clasts is unknown.
790
791   **IMPLICATIONS**
792   Despite decades of mineralogical study of the carbonaceous chondrites, the
793   structural identity and diversity of clay minerals in the CM2 meteorites is only partially
794   resolved. While specific clay mineral components have received in-depth attention, e.g.,
795   cronstedtite (Pignatelli et al. 2018) and polyhedral serpentines (Zega et al. 2006), the
796   structural and elemental diversity that constitutes the bulk clay, which is typically fine-
797   grained and of variable compositions, is less well understood. For example, the diagnostic
798   serpentine d-spacings from the Aguas Zarcas samples above ~30° 2θ do not match those
799   from other Fe- or Mg-rich serpentines, such as chrysotile, ferrous berthierine, odinite, or
800   greenalite (Fig 5). The fact that terrestrial serpentine reflections do not match the d-
801   spacings within the "060" X-ray region is consistent with the statement of Bunch and

802   Chang (1980) - "Adequate identification in terms of terrestrial phyllosilicates nomenclature
803   is precluded by the unique composition and environmental conditions of the meteorite
804   phyllosilicates, slight compositional changes and thermal events. Therefore, it is not
805   surprising that meteoritic phyllosilicates possess their own unique characteristics."
806   Similarly, Zolensky et al. (1993) show that CM chondrite serpentines display a wide range
807   of Fe:Mg ratios, and not two end-members, viz., cronstedtite and antigorite/chrysotile.
808   Further characterization of the clays will necessitate the combined and correlated
809   measurements of TEM and high-spatial-resolution synchrotron XRD.

810   Terrestrial contamination and weathering of meteorites alters and masks their
811   indigenous elemental, mineralogical, isotopic, and in the case of organic-bearing
812   carbonaceous chondrites, their organic inventory. For example, pre-rain stones of the
813   Sutter's Mill C chondrite contain oldhamite, CaS, which is not present in stones collected
814   after wetting by rain (Haberle and Garvie 2017). Even curation of meteorite falls show
815   chemical changes over time (Velbel and Palmer 2011). Isotopic changes can also be rapid,
816   such as the terrestrial weathering and contamination of the hydrogen isotope ratios and
817   H_2O contents of meteoritic minerals (Stephant et al. 2018). The magnitude of terrestrial
818   water-vapor absorption, and hence contamination into the Aguas Zarcas meteorite is shown
819   by the changes in the weight of stones equilibrated in air versus over a drying agent (P_2O_5),
820   suggesting that this meteorite gained ~1.6 wt% of water vapor and other atmospheric
821   contaminants after landing on Earth. However, the rapid collection and curation of many
822   of the Aguas Zarcas stones has preserved their indigenous, extraterrestrial organic
823   inventory (Glavin et al. 2020; Pizzarello et al. 2020), and as shown in this study, their suite
824   of water-soluble compounds (Fig. 8).

825   The NASA OSIRIS-REx mission collected a wealth of material from asteroid
826   101955 Bennu on October 20, 2020, with expected return to Earth in 2023. This asteroid
827   has surface characteristics that indicate mineralogical similarities to CI and CM
828   carbonaceous chondrites, with evidence for widespread hydrated minerals (e.g., Hamilton
829   et al. 2019). The Hayabusa2 mission operated by the Japanese space agency (JAXA)
830   collected samples from asteroid 162173 Ryugu, which were returned to Earth in December,
831   2020. This asteroid too is thought to be carbonaceous chondrite-like and have a surface
832   dominated by hydrous minerals (Kitazato et al. 2019). Clay-rich, and thus aqueously
833   altered meteorites, including the CI and CM chondrites, have been proposed as potential
834   analogues to Ryugu and Bennu. The imminent return of these asteroidal samples has
835   focused scientific attention on the carbonaceous chondrites, especially those with hydrated
836   minerals, such as the serpentines in the CM2 chondrites, and smectite in the CI (King et al.
837   2015), and the recently fallen Tarda (C2-ung) meteorite (Chennaoui Aoudjehane et al.
838   2020). In particular, the study of clay- and organic-rich meteorites, such as Aguas Zarcas,
839   will increase the scientific value of the returned samples. Likewise, the study of the
840   returned sample will also add significantly to our understanding of the meteoritic samples.

841   Mineralogically, the Aguas Zarcas (CM2) meteorite is dominated by serpentine,
842   similar to other CM2 meteorites, whose matrices have phyllosilicate contents of 56 to 89
843   vol% phyllosilicates (Howard et al. 2009; 2015). Powder XRD data from different mm-
844   sized regions shows considerable variations in intensities of reflections for ferrotochilinite
845   and 1:1 regularly interstratified ferrotochilinite/cronstedtite, consistent with this meteorite
846   as a complex breccia. Such brecciation is visible in hand specimens and especially at the
847   SEM scale. This mm-to-mm-scale mineralogical variability is consistent with the
848   brecciation typical for many of the CI and CM chondrites (McCoy et al. 2019; Lentfort et
849   al. 2020; Zolensky et al. 2020), which are interpreted as impact, mainly regolith, breccias.
850   Such brecciation is also widely visible on the boulders of Bennu (McCoy et al. 2019). This
851   fine spatial-scale brecciation necessitates the use of high-spatial-resolution spectroscopic,
852   imaging, X-ray diffraction, and elemental analysis. For example, detailed SEM/EPMA
853   analysis of the Cold Bokkeveld CM2 meteorite reveals a range of CM lithologies including
854   breccia clasts that do not match known meteorite falls or finds. A spectacular example of
855   brecciation is shown by the Kaidun (CR2) meteorite (Zolensky and Ivanov 2003). This
856   meteorite is a microbreccia composed of sub-millimeter-sized clasts representing materials
857   from many different asteroids, principally carbonaceous (CV3, CM1-3, C1, C2), enstatite
858   (EH3-5, EL3), and rumurutite (R) chondrites. The range of clast types reported from the
859   carbonaceous chondrites hints at the diversity likely to be encountered from the returned
860   regolith samples from Ryugu and Bennu. As such, the in-depth, mm-scale mineralogical
861   study of Aguas Zarcas, together with similar studies covering the variety of carbonaceous
862   chondrite meteorites, provides the foundational knowledge with which to interpret and
863   understand the samples returned from Ryugu, Bennu, and future sample return missions.
864
865

866

876   **REFERENCES**

877   Anders, E. and Grevesse, N. (1989) Abundances of the elements. Meteoritic and solar.
878   Geochimica et Cosmochimica Acta, 53, 197-214.

879

880   Aponte, J.C., McLain, H.L., Simkus, D.N., Elsila, J., Glavin, D.P., Parker, E.T. Dworkin,
881   J.P., Hill, D.H., Connolly, H.C.Jr. and Lauretta, D.S. (2020) Extraterrestrial organic
882   compounds and cyanide in the CM2 carbonaceous chondrites Aguas Zarcas and
883   Murchison. Meteoritics and Planetary Science, 1-16.

884

885   Bailey, S.W. (1969) Polytypism of trioctahedral 1:1 layer silicates. Clays and Clay
886   Minerals, 17, 355-371.

887

888   Bailey, S.W. (1981) A system of nomenclature for regular interstratifications. The
889   Canadian Mineralogist, 19, 651-655.

890

891   Bailey, S.W. (1988a) Structures and compositions of other trioctahedral 1:1
892   phyllosilicates. In Hydrous Phyllosilicates (exclusive of micas), S.W. Bailey, editor.
893   Reviews in Mineralogy, 19, 91-167.

894

895   Bailey, S.W. (1988b) Odinite, a new dioctahedral-trioctahedral Fe^{3+}-rich 1:1 clay
896   mineral. Clay Minerals, 23, 237-247.

897

898   Barber, D.J. (1981) Matrix phyllosilicates and associated minerals in C2M carbonaceous
899   chondrites. Geochimica et Cosmochimica Acta, 45, 945-970.

900

901   Brearley, A.J. (2006) The action of water. Pp. 587-624. In: Meteorites and the Early Solar
902   System II. Lauretta, D.S. and McSween, H.Y. (eds), The University of Arizona Press,
903   Arizona, USA.

904

905   Brearley, A.J. and Jones, R.H. (1998) Chondritic meteorites. in Planetary
906   Materials. Papike, JJ (ed.), vol. 36, Reviews in Mineralogy, pp. 3-1 − 3-398.

907

908   Brindley, G.W. (1951) The crystal structure of some chamosite minerals. Mineralogical
909   Magazine, 29, 502-525.

910

911   Brindley, G.W. and Youell, R.F. (1953) Ferrous chamosite and ferric chamosite.
912   Mineralogical Magazine, 30, 57-70.

913

914   Brindley G.W. and Brown G (1984) Crystal Structures of Clay Minerals and their X-ray
915   Identification. Mineralogical Society Monograph No. 5, Mineralogical Society, London.
916   495 pp.

917

918   Bunch, T.E. and Chang, S. (1980) Carbonaceous chondrites – II. Carbonaceous chondrite
919   phyllosilicates and light element geochemistry as indicators of parent body processes and
920   surface conditions. Geochimica et Cosmochimica Acta, 44, 1543-1577.
921

922   Carroll, D. (1970) Clay Minerals: A Guide to their X-ray Identification. Geological
923   Society of America Special Paper, 126, 80 pp.
924

925   Chennaoui Aoudjehane, H., Agee, C., Ziegler, K., Irving, A., Garvie, L.A.J., Sheikh, D.,
926   Carpenter, P., Zolensky, M. and Schmitt-Kopplin, P. (2020) Tarda. Meteoritical Bulletin
927   Database, The Meteoritical Society,
928   https://www.lpi.usra.edu/meteor/metbull.php?code=72644

929

930   Davidson, J., Alexander, C.M.O'D., Bates, H.C., King, A.J., Foustoukos, D.I., Schrader,
931   D.L., Bullock, E.S., Greenwood, R.C., Busemann, H., Morino, P., Riebe, M.E.I.,
932   Rüfenacht, M., Schönbächler, M. and Clay, P. (2020) Coordinated studies of samples
933   relevant for carbonaceous asteroid sample return: CM chondrites Aguas Zarcas and
934   Meteorite Hills 00639. 51st Lunar and Planetary Science Conference, abstract#1623.

935

936   Drits, V.A. and Sakharov, B.A. (1976) X-ray Structural Analysis of Mixed-Layer
937   Minerals. Transactions of the Academy of Sciences of the USSR, Order of the Red
938   Banner of Labor Geological Institute, vol. 295, Responsible Editor B.B. Zvyagin,
939   Moscow (in Russian), 256 pp.

940

941   Fanale, F.P., Li, Y.-H., De Carlo, E., Farley, C., Sharma, S.K., Horton, K. and Granahan,
942   J.C. (2001). An experimental estimate of Europa's "ocean" composition independent of
943   Galileo orbital remote sensing. Journal of Geophysical Research, 106, 14595-14600.

944

945   Fuchs, L.H., Olsen, E., and Jensen, K.J. (1973) Mineralogy, mineral-chemistry, and
946   composition of the Murchison (C2) meteorite. Smithsonian Contributions to the Earth
947   Sciences, 10, 39 pp.

948

949   van der Gaast, S.J. and Vaars, A.J. (1981) A method to eliminate the background in X-
950   ray diffraction patterns of oriented clay mineral samples. Clay Minerals, 16, 383-393.

951

952   Garenne, A., Beck, P., Montes-Hernandez, G., Chiriac, R., Toche, F., Quirico, E., Bonal,
953   L. and Schmitt, B. (2014) The abundance and stability of "water" in type 1 and 2

954   carbonaceous chondrites (CI, CM and CR). Geochimica et Cosmochimica Acta, 137, 93-
955   112.

956

957   Garvie, L.A.J. (1992) Diagenetic tosudite from the lowermost St. Maughan's Group,
958   Lydney Harbour, Forest of Dean, UK. Clay Minerals, 27, 507-513.

959

960   Garvie, L.A.J., Ziegler, K., Soto, G.J., Madrigal, P., Lücke, O. and Farmer, M. (2019)
961   Aguas Zarcas. Meteoritical Bulletin Database, The Meteoritical Society,
962   https://www.lpi.usra.edu/meteor/metbull.php?code=69696

963

964   Garvie, L.A.J., Ziegler, K. and Farmer, M. (2020) Kolang. Meteoritical Bulletin
965   Database, The Meteoritical Society,
966   https://www.lpi.usra.edu/meteor/metbull.php?code=72607

967

968   Gibson, E.K. Jr. and Johnson, S.M. (1972) Thermogravimetric-quadrupole mass-
969   spectrometric analysis of geochemical samples. Thermochimica Acta, 4, 49-56.

970

971   Glavin, D.P., Elsila, J.E., McLain, H.L., Aponte, J.C., Parker, E.T., Dworkin, J.P., Hill,
972   D.H., Connolly Jr. H.C. and Lauretta, D.S. (2020) Extraterrestrial amino acids and L-
973   enantiomeric excesses in the CM2 carbonaceous chondrites Aguas Zarcas and
974   Murchison. Meteoritics and Planetary Science, **DOI:** 10.1111/maps.13451.

975

976   Gooding, J.L. and Zolensky, M.K. (1987) Thermal stability of tochilinite. LPSC XVIII,
977   343-344.

978

979   Greenwood, R.C., Burbine, T.H. and Franchi, I.A. (2020) Linking asteroids and
980   meteorites to the primordial planetesimal population. Geochimica et Cosmochimica Acta,
981   277, 377-406.

982

983   Guggenheim, S., Bailey, S.W., Eggleton, R.A. and Wilkes, P. (1982) Structural aspects of
984   greenalite and related minerals. The Canadian Mineralogist, 20, 1-18.

985

986   Haberle, C.W. and Garvie, L.A.J. (2017) Extraterrestrial formation of oldhamite and
987   portlandite through thermal metamorphism of calcite in the Sutter's Mill carbonaceous
988   chondrite. American Mineralogist, 102, 2415-2421.

989

990   Hamilton, V. E., Simon, A. A., Christensen, P. R., Reuter, D. C., Clark, B. E., Barucci,
991   M. A., Bowles, N. E., Boynton, W. V., Brucato, J. R., Cloutis, E. A., Connolly Jr, H. C.,
992   Donaldson Hanna, K. L., Emery, J. P., Enos, H. L., Fornasier, S., Haberle, C. W., Hanna,
993   R. D., Howell, E. S., Kaplan, H. H., Keller, L. P., Lantz, C., Li, J.-Y., Lim, L. F., McCoy,
994   T. J., Merlin, F., Nolan, M. C., Praet, A., Rozitis, B., Sandford, S. A., Schrader, D. L.,
995   Thomas, C. A., Zou, X.-D., Lauretta, D. S. and the OSIRIS-REx Team (2019) Evidence
996   for widespread hydrated minerals on asteroid (101955) Bennu. Nature Astronomy, 3,
997   332-340.

998

999   Heller-Kallai, L. (1997) The nature of clay volatiles and condensates and the effect on
1000   their environment. A review. Journal of Thermal Analysis, 50, 145-156.

1001

1002   Heller-Kallai, L., Miloslavski, I. and Aizenshtat, Z. (1987) Volatile products of clay
1003   mineral pyrolysis revealed by their effect on calcite. Clay Minerals, 22, 339-348.

1004

1005   Heller-Kallai, L., Miloslavski, I., Aizenshtat, Z. and Halicz, L. (1988) Chemical and mass
1006   spectrometric analysis of volatiles derived from clays. American Mineralogist, 73, 376-
1007   382.

1008

1009   Howard, K.T., Benedix, G.K., Bland, P.A. and Cressey, G. (2009). Modal mineralogy of
1010   CM2 chondrites by X-ray diffraction (PSD-XRD). Part 1: Total phyllosilicate abundance
1011   and the degree of aqueous alteration. Geochimica et Cosmochimica Acta, 73, 4576-4589.

1012

1013   Howard, K.T., Alexander, C.M.O'D., Schrader, D.L. and Dyl, K.A. (2011) Classification
1014   of hydrous meteorites (Cr, CM and C2 ungrouped) by phyllosilicate fraction: PSD-XRD
1015   modal mineralogy and planetesimal environments. Geochimica et Cosmochimica Acta,
1016   149, 206-222.

1017

1018   Hybler, J. (2006) Parallel intergrowths in cronstedtite-1T: determination of the degree of
1019   disorder. European Journal of Mineralogy, 18, 197-205.

1020

1021   Hybler, J. (2014) Refinement of cronstedtite – 1M. Acta Crystallographica B70, 963-972.

1022

1023   King, A.J., Bates, H.C., Krietsch, D., Busemann, H., Clay, P.L. and Russell, S.S. (2019)
1024   The Yamato-type (CY) carbonaceous chondrite group: Analogues for the surface of
1025   asteroid Ryugu? Geochemistry, 79, 125531.

1026

1027   Irving, A.J., Kuehner, S.M., Rumble III, D., Korotev, R.L. and Clary, S. (2009) Moapa
1028   Valley: A second non-Antarctic CM1 chondrite from Nevada, USA. 72nd Annual
1029   Meteoritical Society Meeting, Abstract#5372.

1030

1031   ten Kate, I.L., Cardiff, E.H., Dworkin, J.P., Feng, S.H., Holmes, V., Malespin, C., Stern,
1032   J.G., Swindle, T.D. and Glavin, D.P. (2010) VAPoR – Volatile Analysis by Pyrolysis of
1033   Regolith – an instrument for in situ detection of water, noble gases, and organics on the
1034   Moon. Planetary and Space Science, 58, 1007-1017.

1035

1036   Kebukawa, Y., Nakashima, S. and Zolensky, M.E. (2010) Kinetics of organic matter
1037   degradation in the Murchison meteorite for the evaluation of parent-body temperature
1038   history. Meteoritics and Planetary Science, 45, 99-113.

1039

1040   Kebukawa, Y., Zolensly, M.E., Mathurin, J., Dartois, E., Engrand, C., Duprat, J.,
1041   Deniset-Besseau, A., Dazzi, A., Fries, M., Ohigashi, T., Wakabayashi, D., Yamashita, S.,
1042   Takeichi, Y., Takahashi, Y., Kondo, M., Ito, M., Kodama, Y., Rahman, Z. and
1043   Kobayashi, K. (2020) Organic matter in the Aguas Zarcas (CM2) meteorite: High

1044   abundance of aliphatic carbon in metal-rich lithology. 51st Lunar and Planetary Science
1045   Conference. Abstract#1349.
1046
1047   Kerraouch, I., Bishoff, A., Zolensky, M.E., Pack, A., Patzek, M., Wölfer, E., Burkhardt,
1048   C. and Fries, M. (2020) Characteristics of a new carbonaceous, metal-rich lithology
1049   found in the carbonaceous chondrite breccia Aguas Zarcas. 51st Lunar and Planetary
1050   Science Conference. Abstract#2011.
1051
1052   Kerridge, J.F., Chang, S. and Shipp, R. (1987) Isotopic characterization of kerogen-like
1053   materials in the Murchison carbonaceous chondrite. Geochimica et Cosmochimica Acta,
1054   51, 2527-2540.
1055
1056   King, T.V.V. and King, E.A. (1981) Accretionary dark rims in unequilibrated chondrites.
1057   Icarus, 48, 460-472.
1058
1059   King, A.J., Schofield, P.F. and Russell, S.S. (2015) Modal mineralogy of CI and CI-like
1060   chondrites by X-ray diffraction. Geochimica et Cosmochimica Acta, 165, 148-160.
1061
1062   Kitazato, K., Milliken, R. E., Iwata, T., Abe, M., Ohtake, M., Matsuura, Arai, S.,T.,
1063   Nakauchi, Y., Nakamura, T., Matsuoka, M., Senshu, H., Hirata, N., Hiroi, T., Pilorget,
1064   C., Brunetto, R., Poulet, F., Riu, L., Bibring, J.-P., Takir, D., Domingue, D. L., Vilas, F.,
1065   Barucci, M. A., Perna, D., Palomba, E., Galiano, A., Tsumura, K., Osawa, T., Komatsu,
1066   M., Nakato, A., Arai, T., Takato, N., Matsunaga, T., Takagi, Y., Matsumoto, K.,
1067   Kouyama, T., Yokota, Y., Tatsumi, E., Sakatani, N., Yamamoto, Y., Okada, T., Sugita,
1068   S., Honda, R., Morota, T., Kameda, S., Sawada, H., Honda, C., Yamada, M., Suzuki, H.,
1069   Yoshioka, K., Hayakawa, M., Ogawa, K., Cho, Y., Shirai, K., Shimaki, Y., Hirata, N.,
1070   Yamaguchi, A., Ogawa, N., Terui, F., Yamaguchi, T., Takei, Y., Saiki, T., Nakazawa, S.,
1071   Tanaka, S., Yoshikawa, M., Watanabe, S. and Tsuda, Y. (2019) The surface composition
1072   of asteroid 162173 Ryugu from Hayabusa 2 near-infrared spectroscopy. Science, 364,
1073   272-275.
1074
1075   Kouvatsis, I. and Cartwright, J.A. (2020) The Aguas Zarcas meteorite: A review of
1076   chondrules and fine-grained rims observed with a new carbonaceous chondrite (CM2)
1077   fall. 51st Lunar and Planetary Science Conference, abstract#2512.
1078
1079   Kozerenko, S.V., Fadeev, V.V., Organova, N.I., Chistyakova, N.I., Kolpakova, N.N., and
1080   Senin, V.G. (2001) Synthesis, formation conditions and crystallochemistry of tochilinites
1081   – iron, magnesium and sodium hydroxide-sulfides. Experimental Geosciences, 10, 57-58.
1082
1083   Kvenvolden, K., Lawless, J., Pering, K., Peterson, E., Flores, J., Ponnamperuma, C.,
1084   Kaplan, I. R. and Moore, C. (1970) Evidence for extraterrestrial amino-acids and
1085   hydrocarbons in the Murchison meteorite. Nature, 228, 923−926.
1086

1087   Lauretta, D.S. et al. (2019) The unexpected surface of asteroid (101955) Bennu. Nature
1088   568, 55-60.

1089

1090   Lentfort, S., Bischoff, A., Ebert, S. and Patzek, M. (2020) Classification of CM chondrite
1091   breccias – Implications for the evaluation of samples from ORIRIS-REx and Hayabasu 2
1092   missions. Meteoritics and Planetary Science, 1-21, doi: 10.1111/maps.13486.

1093

1094   Lücke, O. H., Madrigal, P. and Soto, G. J. (2019) El condrito carbonáceo Aguas Zarcas:
1095   bólido, caída y recuperación de un meteorito extraordinario del tipo CM2. Revista
1096   Geológica de América Central, 60, 9–22. doi:10.15517/RGAC.V61I0.40085

1097

1098   Mackinnon, I.D.R. and Zolensky, M.E. (1984) Proposed structures for poorly
1099   characterized phases in C2M carbonaceous chondrites. Nature, 309, 240-242.

1100

1101   McCoy, T.J., Connolly Jr., H.C., Corrigan, C.M., Jawin, E.R., Sandford, S., Molaro, J.,
1102   DellaGiustina, D.N., Bizk, B., Nolan, M.C., Lauretta, D.S. and OSIRIS-REx Team.
1103   (2019) Brecciated boulders: evidence for impact mixing on Bennu's parent body. 82nd
1104   Annual Meeting of The Meteoritical Society 2019 (LPI Contrib. No. 2157)

1105

1106   McKee, T.R. and Moore, C.B. (1979) Characterization of submicron matrix
1107   phyllosilicates from Murray and Nogoya carbonaceous chondrites. Proceedings of the
1108   Lunar and Planetary Science Conference 10th, 921-935.

1109

1110   Kelsey, L. and Lauretta, D.S. (2013) Purifying water mined from asteroids for in situ
1111   resource utilization. Meteoritical Society Proceedings, pp 21.

1112

1113   Metzler, K., Bischoff, A. and Stöffler, D. (1992) Accretionary dust mantles in CM
1114   chondrites: Evidence for solar nebula processes. Geochemica et Cosmochimica Acta, 56,
1115   2873-2897.

1116

1117   Moore, D.M. and Reynolds, R.C. Jr. (1989) X-ray Diffraction and the Identification and
1118   Analysis of Clay Minerals. Oxford University Press, Inc., New York, 332 pp.

1119

1120   Morris, A.A., Baker, L., Franchi, I.A. and Wright, I.P. (2005) Evolved gas analysis of
1121   hydrated phases in Murchison and Orgueil. 36th Lunar and Planetary Science Conference,
1122   abstract#1925.

1123

1124   Morris, R.V., Clark, J.V., Lee, S., Keller, L.P., Agresti, D.G., and Archer, P.D., Jr. (2020)
1125   X-ray diffraction and reflectance spectroscopy of Murchison powders (CM2) after
1126   thermal analysis under reducing conditions to final temperatures between 300 and 1300
1127   °C. 51st Lunar and Planetary Science Conference.

1128

1129   Nakamura, T. and Nakamuta, Y. (1996) X-ray study of PCP from the Murchison CM
1130   carbonaceous chondrite. Proceedings of the NIPR Symposium on Antarctic Meteorites, 9,
1131   37-50.

1132

1133 Newman, A.C.D. and Brown, G. (1987) The Chemical Constitution of Clays. In.
1134 Chemistry of Clays and Clay Minerals. A.C.D. Newman (ed), Mineralogical Society
1135 Monograph No. 6, p 1-128. Great Britain, The Bath Press, Avon.

1136
1137 Nickel, E.H. and Grice, J.D. (1998) The IMA Commission on New Minerals and Mineral
1138 Names: procedures and guidelines on mineral nomenclature, 1998. The Canadian
1139 Mineralogist, 36, 913-926.

1140
1141 Organova, N.I., Drits, V.A. and Dmitrik, A.L. (1973) Structural study of tochilinite. Part
1142 1. The isometric variety. Soviet Physics − Crystallography, 17, 667-671.

1143
1144 Organova, N. I., Gorshkov, A. I., Dikov, Y. P., Kul'bachinskiy, V. A., Laputina, I. P.,
1145 Sivtsov, A. V., Sluzhenikin, S. F. and Ponomarenko, A. I. (1988) The new data on
1146 tochilinite. International Geology Review, 6, 84–98.

1147
1148 Pekov, I.V., Sereda, E.V., Polekhovksy, Yu.S., Britvin, S.N., Chukanov, N.V.,
1149 Yapaskurt, V.O. and Bryzgalov, I.A. (2013) Ferrotochilinite, $6FeS.5Fe(OH)_2$, a new
1150 mineral of the Oktyabr'sky deposit, Noril'sk district, Siberia, Russia. Geology of Ore
1151 Deposits, 53. 567-574.

1152
1153 Pignatelli, I., Mugnaioli, E. and Marrocchi, Y. (2018) Cronstedtite polytypes in the Paris
1154 Meteorite. European Journal of Mineralogy, 30, 349-354.

1155
1156 Pizzarello, S. and Huang, Y. (2005) The deuterium enrichment of individual amino acids
1157 in carbonaceous meteorites: A case for the presolar distribution of biomolecule
1158 precursors. Geochimica et Cosmochimica Acta 69:599–605.

1159
1160 Pizzarello S., Cooper G. W., and Flynn G. J. (2006) The nature and distribution of the
1161 organic material in carbonaceous chondrites and interplanetary dust particles. In
1162 Meteorites and the early solar system II, edited by Lauretta D., Leshin L. A., and
1163 McSween H.Y. Jr. Tucson, Arizona: University of Arizona Press. pp. 625–651.

1164
1165 Pizzarello S. and Garvie L.A.G. (2014) Sutter's Mill dicarboxylic acids as possible tracers
1166 of parent-body alteration processes. Meteoritics and Planetary Science, 49, 2087–2094.

1167
1168 Pizzarello, S., Yarnes, C.T. and Cooper, G. (2020) The Aguas Zarcas (CM2) meteorite:
1169 New insights into early solar system organic chemistry. Meteoritics and Planetary
1170 Science, 55, 1-14.

1171
1172 Schmitt-Kopplin P., Gabelica Z., Gougeon R. D., Fekete A., Kanawati B., Harir M.,
1173 Gebefuegi I., Eckel G. and Hertkorn N. (2010) High molecular diversity of
1174 extraterrestrial organic matter in Murchison meteorite revealed 40 years after its fall.
1175 Proceedings of the National Academy of Sciences 107:273–2768.

1176
1177 Sephton M. A. (2002) Organic compounds in carbonaceous meteorites. National Product
1178 Reports 19:292–311.

1179
1180   Smykatz-Kloss, W. (1974) Differential Thermal Analysis. Application and Results in
1181   Mineralogy (Minerals and Rocks, vol. II). Berlin, Heidelberg, and New York. Springer-
1182   Verlag, 185 pp.
1183
1184   Springmann, A., Lauretta, D.S., Klaue, B., Goreva, Y.S., Blum, J.D. Andronikov, A. and
1185   Steckloff, J.K. (2019) Thermal alteration of labile elements in carbonaceous chondrites.
1186   Icarus, 324, 104-119.
1187
1188   Stephant, A., Garvie, L.A.J., Mane, P., Hervig, R. and Wadhwa, M. (2018) Terrestrial
1189   exposure of a fresh Martian meteorite causes rapid changes in hydrogen isotopes and
1190   water concentrations. Scientific Reports, 8:12385.
1191
1192   Takir, D., Howard, K.T., Stockstill-Cahill, K.R., Hibbitts, C.A., Abreu, N., Zolensky,
1193   M.E. and Fries, M. (2020) Spectroscopy and mineralogy of Aguas Zarcas. 51st Lunar and
1194   Planetary Science Conference, Abstract#2533.
1195
1196   Vacher, L.G., Truche, L., Faure, F., Tissandier, L., Mosser-Ruck, R. and Marrocchi, Y.
1197   (2019) Deciphering the conditions of tochilinite and cronstedtite formation in CM
1198   chondrites from low temperature hydrothermal experiments. Meteoritics and Planetary
1199   Science, 54, 1870-1889.
1200
1201   Vacher, L.G., Piani, L., Rigaudier, T., Thomassin, D., Florin, G., Piralla, M. and
1202   Marrocchi, Y. (2020) Hydrogen in chondrites: influence of parent body alteration and
1203   atmospheric contamination on primordial components. Geochimica et Cosmochimica
1204   Acta, 284, 53-66.
1205
1206   Velbel, M.A. (1988) The distribution and significance of evaporitic weathering products
1207   on Antarctic meteorites. Meteoritics, 23, 151-159.
1208
1209   Velbel, M.A. and Palmer, E.E. (2011) Fine-grained serpentine in CM2 carbonaceous
1210   chondrites and its implications for the extent of aqueous alteration on the parent body: A
1211   review. Clays and Clay Minerals, 59, 416-432.
1212
1213   Verchovsky, A.B., Anand, M., Barber, S.J., Sheridan, S. and Morgan, G.H. (2020) A
1214   quantitative evolved gas analysis for extra-terrestrial samples. Planetary and Space
1215   Science, 181, 104830.
1216
1217   Wasson, J.T. and Kallemeyn, G.W. (1988) Composition of chondrites. Philosophical
1218   Transactions of the Royal Society of London A325, 535-544.
1219
1220   Weisberg, M.K., McCoy, T.J. and Krot, A.N. (2006) Systematics and evaluation of
1221   meteorite classification. Pp. 19-52. In: Meteorites and the Early Solar System II. Lauretta,
1222   D.S. and McSween, H.Y. (eds), The University of Arizona Press, Arizona, USA.
1223

1224

1225   Wicks, F.J. and O'Hanley, D.S. (1988) Serpentine minerals: Structures and petrology. In
1226   Hydrous Phyllosilicates (exclusive of micas), S.W. Bailey, editor. Reviews in
1227   Mineralogy, 19, 91-167.

1228
1229   Wilson, M.J. (1987) X-ray powder diffraction methods. In A Handbook of Determinative
1230   Methods in Clay Mineralogy, M.J. Wilson, ed., Blackie & Son Ltd., Glasgow and
1231   London, 26-98.

1232
1233   Whitney, G. and Eberl, D.D. (1982) Mineral paragenesis in a talc-water experimental
1234   hydrothermal system. American Mineralogist, 67, 944-949.

1235
1236   Zega, T.J. and Buseck, P.R. (2003) Fine-grained-rim mineralogy of the Cold Bokkeveld
1237   CM chondrite. Geochimica et Cosmochimica Acta, 67, 1711-1721.

1238
1239   Zega, T.J., Garvie, L.A.J. and Buseck, P.R. (2003) Nanometer-scale measurements of
1240   iron oxidation states of cronstedtite from primitive meteorites. American Mineralogist,
1241   88, 1169-1172.

1242
1243   Zega, T.J., Garvie, L.A.J., Dódony, I. and Buseck, P.R. (2004) Serpentine nanotubes in
1244   the Mighei CM chondrite. Earth and Planetary Science Letters, 223, 141-146.

1245
1246   Zega, T.J., Garvie, L.A.J., Dódony, I., Friedrich, H., Stroud, R.M. and Buseck, P.R.
1247   (2006) Polyhedral serpentine grains in CM chondrites. Meteoritics and Planetary
1248   Sciences, 41, 681-688.

1249
1250   Zolensky, M., Barrett, R. and Browning, L. (1993) Mineralogy and composition of
1251   matrix and chondrules rims in carbonaceous chondrites. Geochimica et Cosmochimica
1252   Acta, 57, 3123-3148.

1253
1254   Zolensky, M. and Ivonov, A. (2003) The Kaidun microbreccia meteorite: a harvest from
1255   the inner and outer asteroid belt. Chemie der Erde Geochemistry, 63, 185-246.

1256
1257   Zolensky, M., Velbel, M. and Le, L. (2020) Brecciation of CM chondrites: Cold
1258   Bokkeveld. 51st Lunar and Planetary Science Conference, abstract#1946.

1259
1260   Zolotov, M.Yu., Zolotova, N.B. and Romaniello, S.J. (2018) Water extraction from
1261   Murchison CM2 chondrite: trace metals and major ions. 81st Annual Meeting of The
1262   Meteoritical Society 2018 (LPI Contrib. No. 2067), abstract#6340.

1263

1264

1265
1266
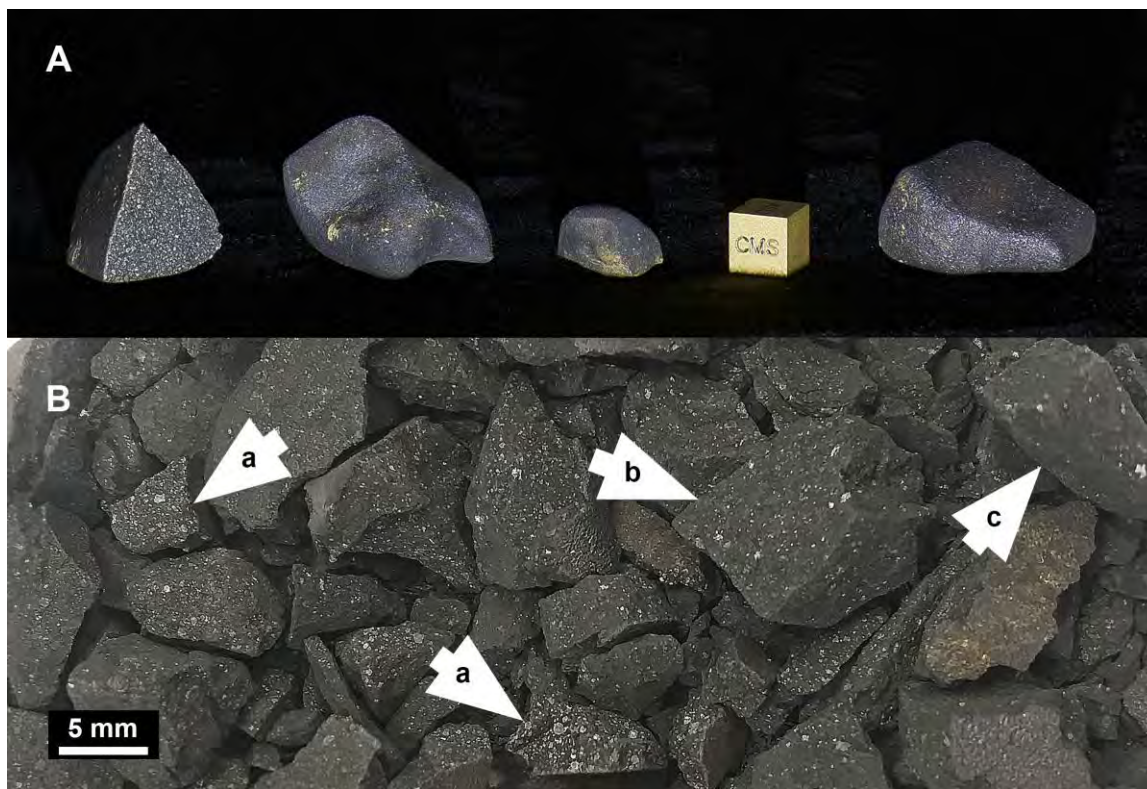
1267
1268
1269
1270 **Figure 1**. **A**) Photograph of four Aguas Zarcas stones in the Center for Meteorite Studies.
1271 From left to right – 10.49 g (ASU#2121_1), 18.07 g (ASU#2121_4), 3.41 g (ASU#2121_2,
1272 and 17.73 g (ASU#2121_2). 1-cm scale cube for comparison. Stones donated to the CMS
1273 by Carleton Moore. **B**) Photograph of a collection of fragments showing the three dominant
1274 lithologies – **a**) chondrule rich, **b**) chondrule poor, and **c**) "matrix lithology" bearing few
1275 chondrules.
1276
1277
1278

1279
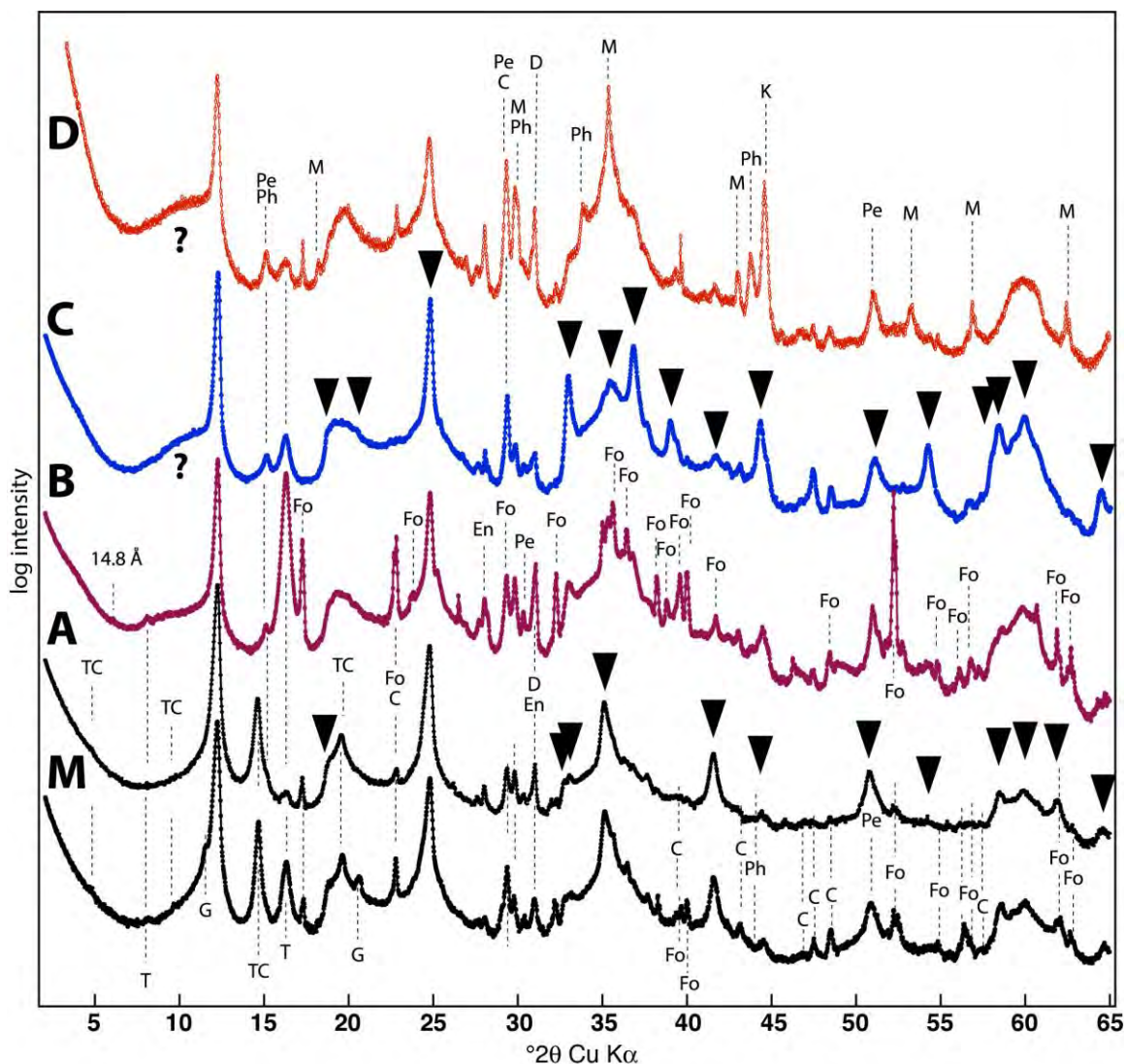
1280
1281
1282 **Figure 2**. Powder XRD patterns from four Aguas Zarcas fragments **A)** Typical chondrule-
1283 poor fragment from #2121_5, **B)** chondrule-poor fragment from #2121_6, **C)** 5-mm clast
1284 of matrix-rich lithology from stone #2121_5, and **D)** metal-rich lithology from stone
1285 #2121_16 compared with a typical pattern from **M)** Murchison. Pe – pentlandite, Ph –
1286 pyrrhotite, T – ferrotochilinite, TC – 1:1 regularly interstratified
1287 ferrotochilinite/cronstedtite, Fo – forsterite, En – enstatite, C – calcite, D – dolomite, K –
1288 kamacite, G – gypsum, and M - magnetite. ? – broad low-angle hump centered at 8.56 Å.

1289 Serpentine reflections indicated by a ▼ (See Table 1). Murchison is from stone
1290 ASU#828_33.

1291
1292

1293
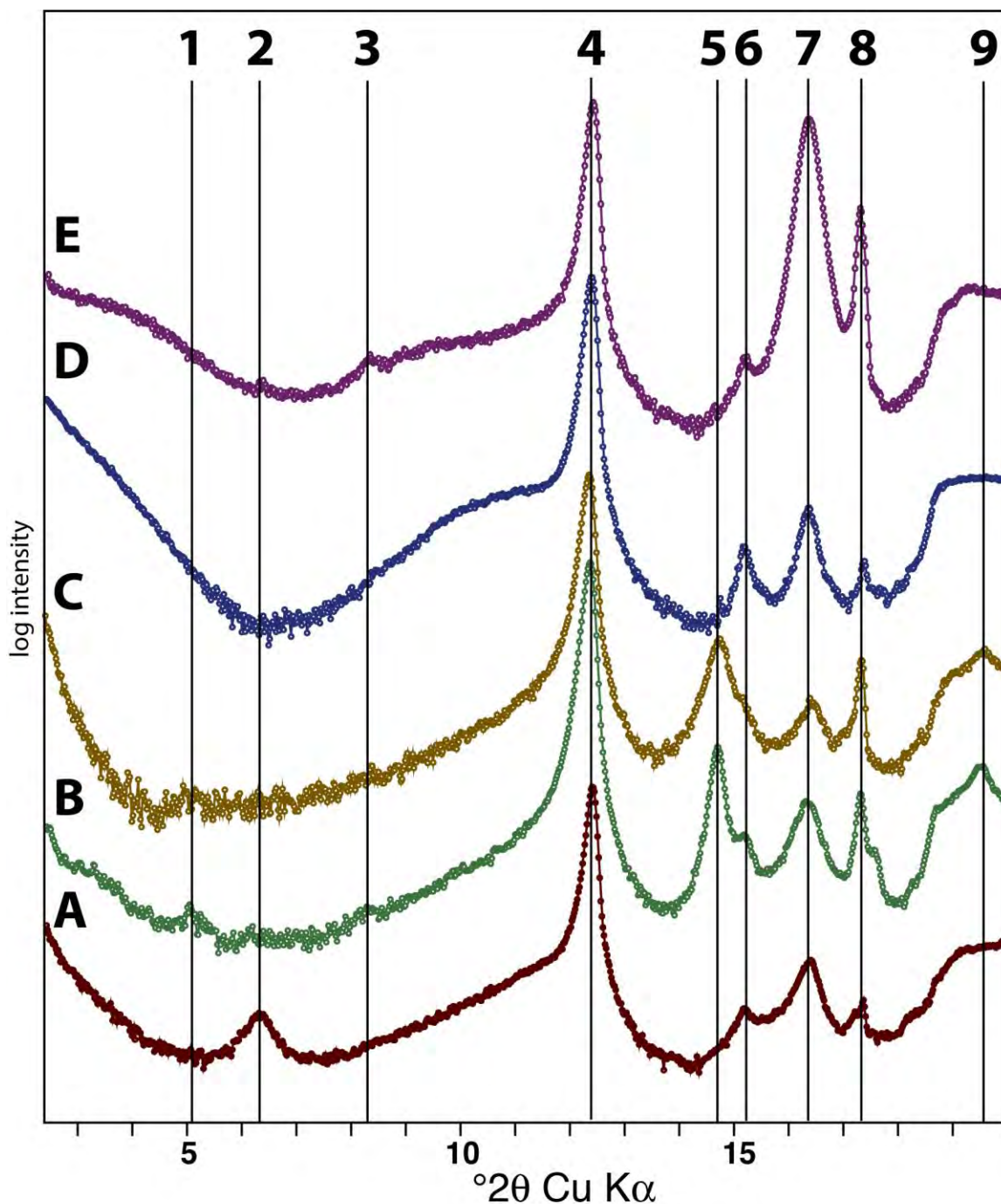
1294

1295 **Figure 3**. Powder XRD patterns from Aguas Zarcas showing the weaker reflections in the
1296 2° to 20° 2θ region on a log intensity scale and after background subtraction. **A)** chondrule-
1297 free clast (#2121_17); **B)** typical fragment (#2121_5); **C)** chondrule-poor clast (#2121_13);
1298 **D)** chondrule-poor chip (#2121_7); **E)** chondrule-poor clast (#2121_6). The d-spacings for
1299 1 to 9 are – **1)** 18.3 Å, **2)** 14.76 Å, **3)** 10.8 Å, **4)** 7.26 to 7.23 Å, **5)** 6.05 Å, **6)** 5.856 Å, **7)**
1300 5.4 Å, **8)** 5.13 Å, and **9)** 4.54 Å

1301

1302
1303
1304
1305
1306
1307
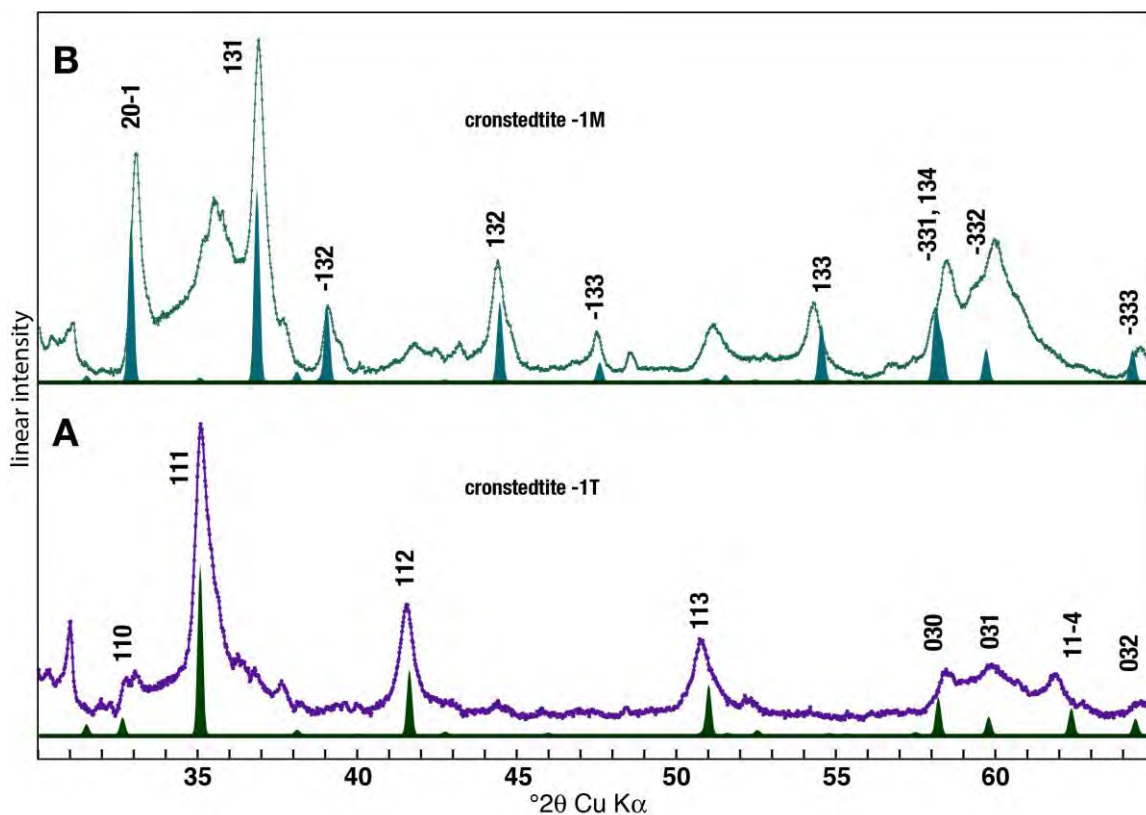
1308
1309
1310 **Figure 4**. Powder X-ray diffraction patterns from 30° to 65° 2θ for **A)** Typical chondrule-
1311 poor fragment from #2121_5, and **B)** 5-mm clast of matrix-rich lithology from stone
1312 #2121_5 (both shown over a larger 2θ range in Fig. 2). The background has been subtracted
1313 from beneath the experimental patterns. The simulated patterns for cronstedtite 1T and 1M
1314 are shown as filled reflections beneath each pattern. Reflections with relative intensities of
1315 >10% are indexed. Structure data used to calculate the simulated patterns are from Hybler
1316 2006 and 2014.
1317
1318

1319
1320
1321
1322
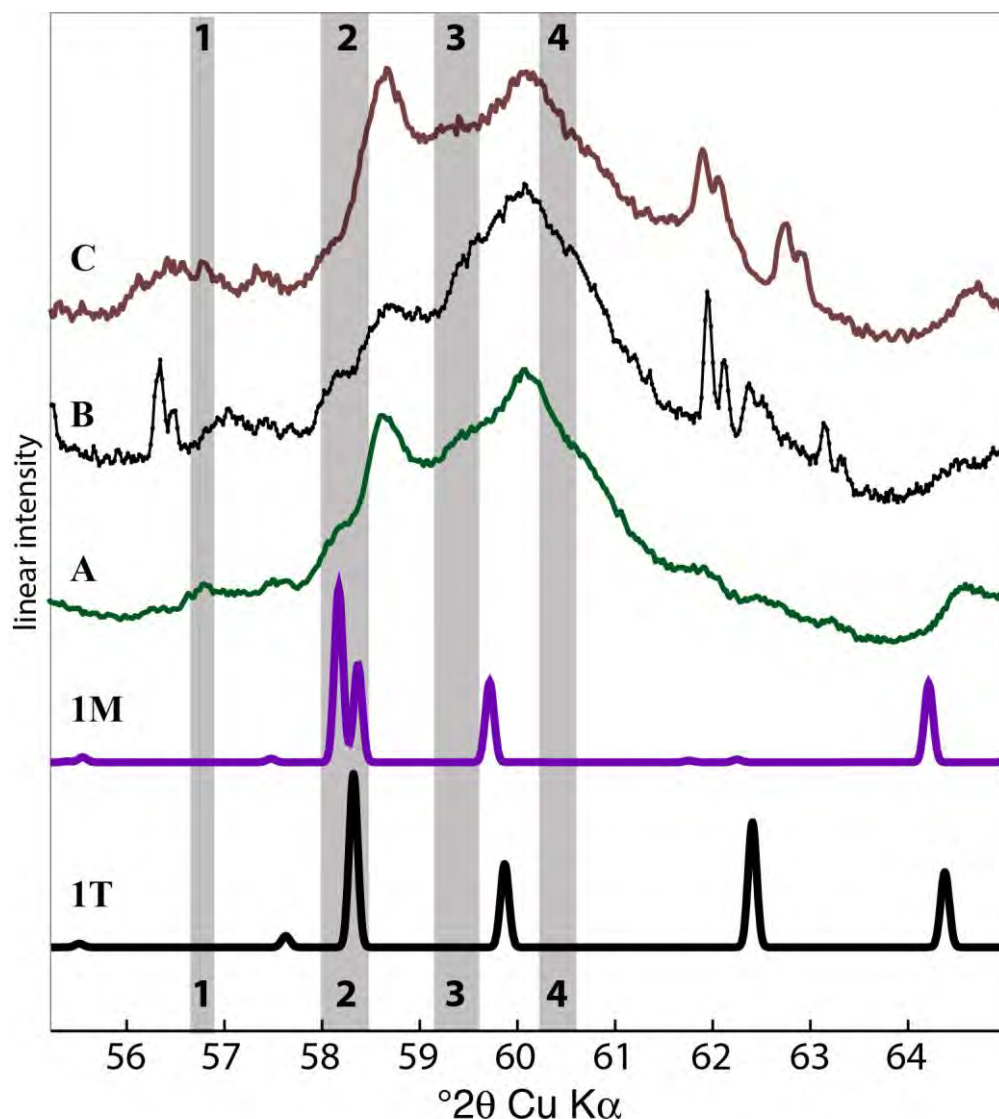
1323
1324

Figure 5. Comparison of the simulated XRD profiles for 1T and 1M cronstedtite within the "060" X-ray diffraction region for Aguas Zarcas patterns **A)** matrix-rich lithology, **B)** chondrule-free clast (#2121_17), and **C)** typical chondrule-poor fragment. The shaded bars show the 2θ ranges for the major reflections from selected Fe- and Mg-rich serpentine group minerals listed in Table 3. **1** – greenalite, **2** – cronstedtite, **3** – odinite and berthierine, and **4** – chrysotile and amesite. The sharp reflections in **A)** and **B)** between 61.5° and 63° 2θ are from forsterite and split into $K\alpha_1$ and $K\alpha_2$ components.

1332
1333

1334
1335
1336
1337
1338
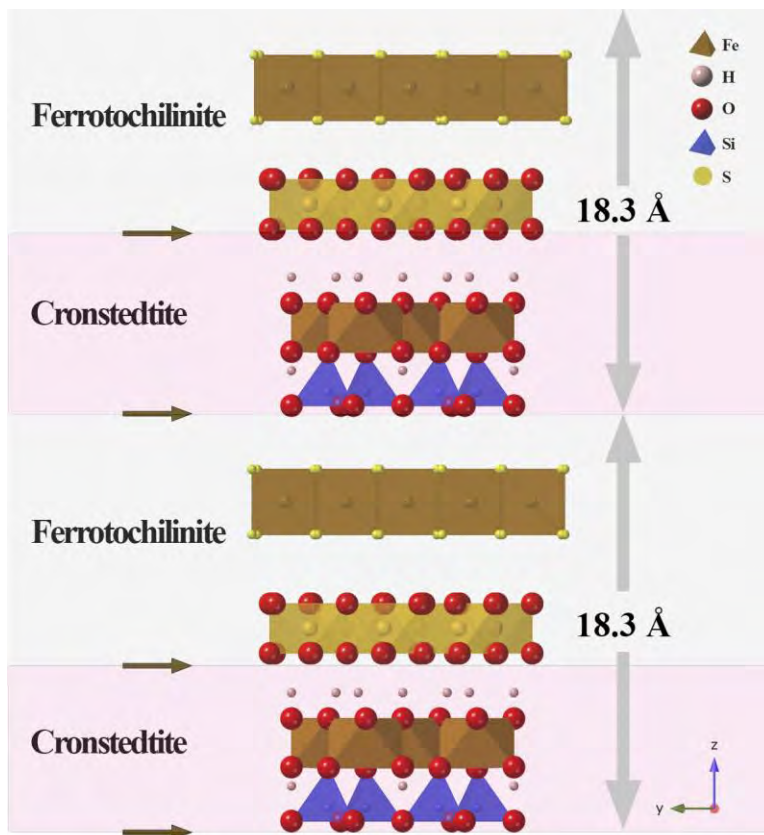
1339
1340
1341
1342   Figure 6. Cartoon structure model showing the regular 1:1 interstratification along the c-
1343   direction of cronstedtite and ferrotochilinite that gives rise to the 18.3 Å reflection.
1344   Cronstedtite structure for the 1T polytype from Hybler 2006. Tochilinite structure from
1345   Organova et al. 1973. H atoms shown for cronstedtite, though none are shown for the
1346   tochilinite as their positions were not refined. The origin of the 18.3 Å superlattice
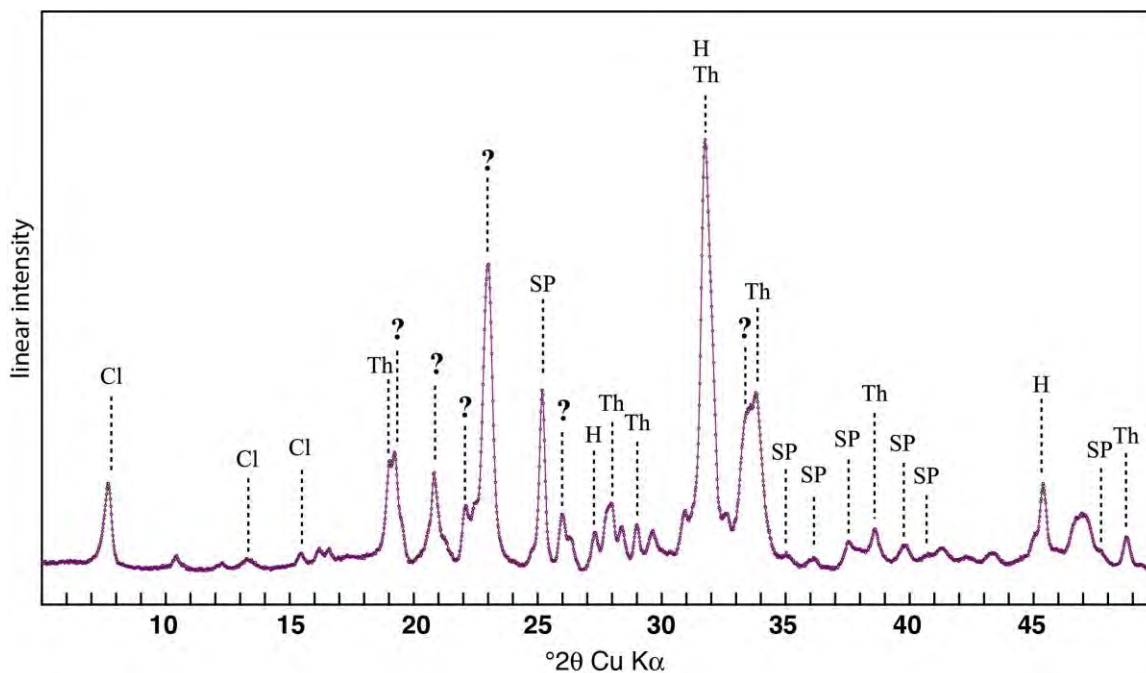1347   reflection is indicated.
1348

1349
1350
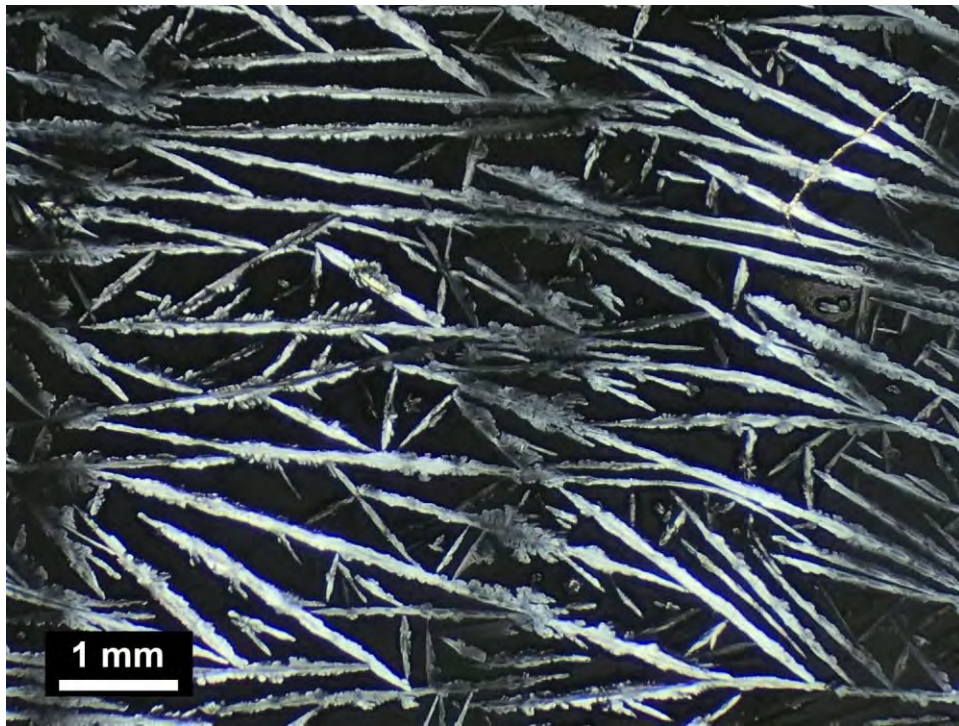
1351
1352
1353   **Figure 7**. Transmitted-light, crossed-polarized photograph of the dried water extract from
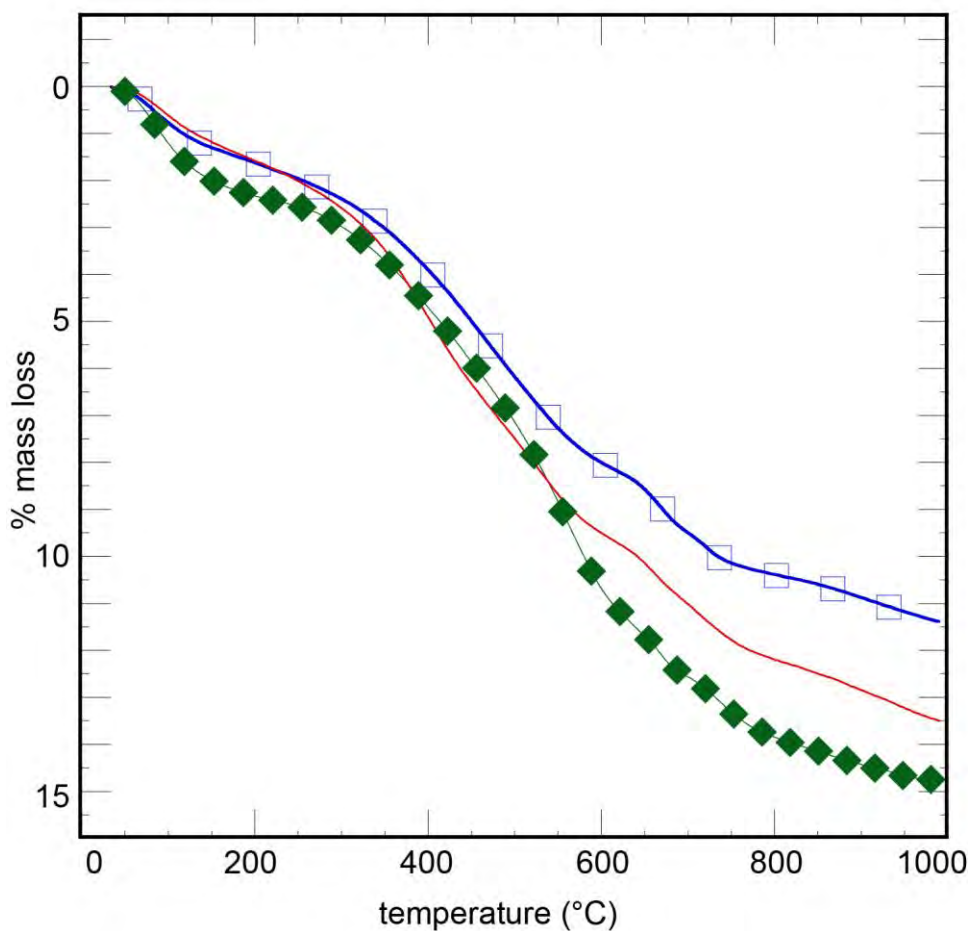1354   Aguas Zarcas stone #2121_6 crystallized onto a glass slide.
1355
1356
1357

1358
1359
1360
1361
1362
1363
1364

1365
1366

Figure 8. Powder XRD pattern of the dried crystallized water extract from stone #2121_6. Cl – partially hydrated chlorartinite, Th – thenardite, SP – sodium perchlorate, H – halite. ? – unmatched major reflection.
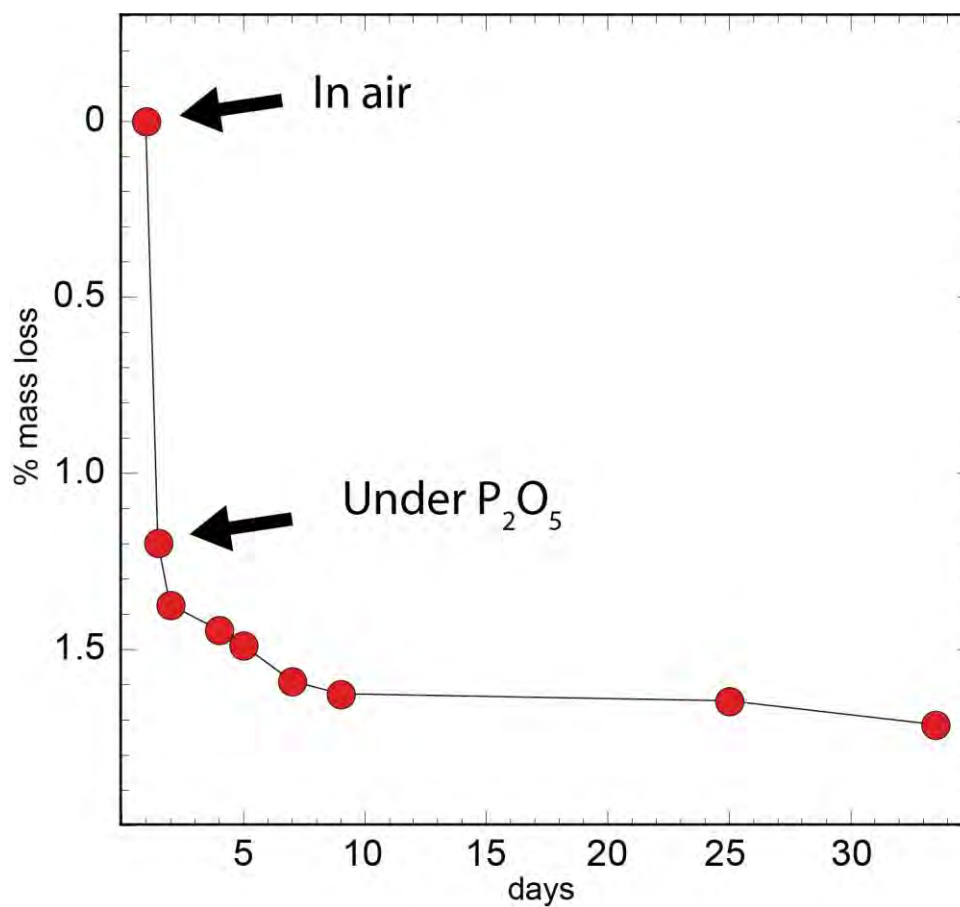
1370
1371
1372

1373
1374
1375

1376
1377
1378 Figure 9. Thermogravimetric (TG) data for three representative fragments of Aguas Zarcas
1379 – green diamonds, matrix-rich lithology (#2121_7), red line, chondrule-poor lithology
1380 (#2121_5), and blue squares, chondrule-rich lithology (#2121_8).
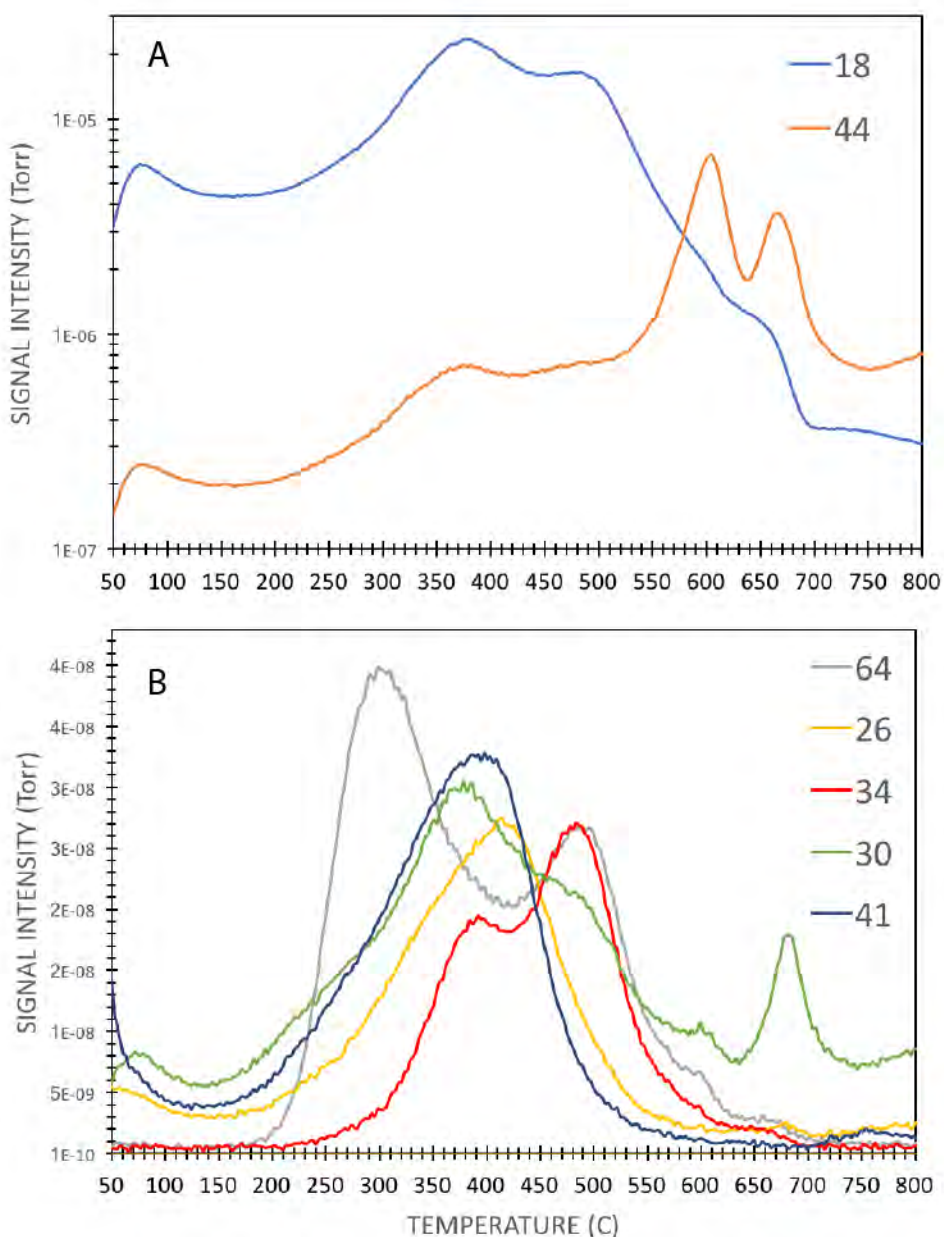1381
1382
1383

1384

1385
1386
1387 **Figure 10**. Weight percent mass loss of a 5.2745 g fragment of stone #2121_5 after being
1388 placed in a desiccator containing the P_2O_5 drying agent.
1389
1390
1391

1392

1393
1394
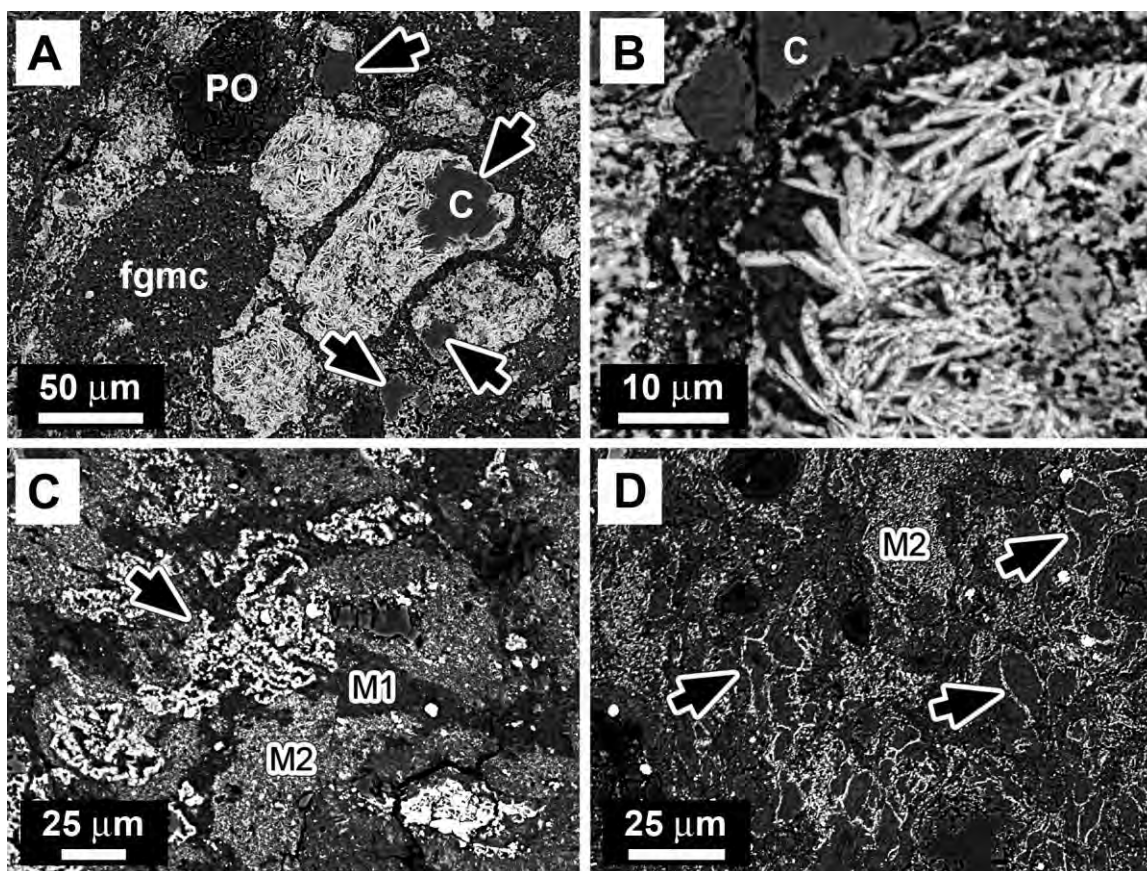1395 **Figure 11**. Evolved Gas Analysis (EGA) data of a fragment of stone #2121_5 as a function
1396 of temperature. **A**) Comparison of masses corresponding to the two most abundant gases
1397 H_2O (18) and CO_2 (44) on a logarithmic scale. **B**) Selected gases with m/z masses of 64 –
1398 SO_2, S_2; 26 – C_2H_2; 34 – H_2S; 30 – HCOH, C_2H_6.
1399
1400
1401

1402

1403
1404
Figure 12. Back-scattered-electron (BSE) images of representative areas of Aguas Zarcas
matrix. **A**) Stone #2121_5 is chondrule poor and is the "average" lithology of many of the
stones. It is locally dominated by bright TCI clasts, fine-grained matrix clasts (fgmc),
separated by a low-Z matrix. Arrows point to calcite grains. PO – porphyritic olivine
chondrule. C – calcite. **B**) Higher magnification of a bright TCI clast showing the bladed
habit of the Fe-S-Mg-rich grains. **C**) Typical area of the "matrix-rich lithology" from a 4.3
g stone (#2121_7). This stone shows three distinct matrix components, viz., dark (M1),
which is relatively Mg-rich and Fe-poor; medium bright and speckled (M2), and bright
sinuous connected network of Fe-S-rich material (arrow). **D**) Typical matrix of the metal-
rich area from chondrule-rich stone #2121_8, showing dark clasts with bright rims
(arrowed clasts) and a speckled lithology (M2).

1416
1417
1418
1419

1420

1421 **Table 1**. Comparison of the d-spacings (Å) of the serpentine reflections measured from

1422 the powder XRD patterns from two Aguas Zarcas fragments, compared with data from

1423 Murchison.

1424

#2121_5; chondrule-poor clast			#2121_5; matrix-rich lithology			Murchison (this study)		Murchison (Fuchs et al. 73)	
d(Å)	I	Assign-ments	d(Å)	I	Assign-ments	d(Å)	I	d(Å)	I
7.248	10	S	7.240	10	S	7.22	10	7.2	10
4.74	1	S	4.74	02-prism	S	4.72	02-prism	4.7	02-prism
3.590	4	S	3.582	5	S	3.587	4	3.58	5
2.732	1	1T,1M	2.711	3	1M	2.731	2U	2.7	2
2.714	1					2.710	2		
2.552	3	1T	2.551	2U	1T	2.548	3	2.53	8
2.436	1	1M	2.437	4	1M	2.439	2B	2.43	3
-	-	-	2.311	2	1M	-	-	2.30	1
			2.290	1S					
2.170	2	1T	2.166	1B	1T	2.169	2	2.16	4
2.04	1B	1M	2.042	2	1M	2.03	1	2.03	1
			2.028	1U					
-	-	-	1.914	1	1M	-	-	-	-
1.795	2	1T	1.786	2B	1M	1.792	2	1.79	2
-	-	-	1.692[#]	2	1M	-	-	-	-
1.584	2U	1T	1.586	2U	1M	-	-	-	-
1.575	3	S	1.575	3	S	1.572	3	1.57	3
-	-	-	1.554	2U	1M	-	-	-	-
1.542	3	S	1.539	3	S	1.538	3	1.54	3
-	-	-	1.524	1B	S	1.521	1B	-	-
1.497	1	S	-	-	-	1.497	1	1.49	1
1.441	1	1T	1.444	2	1M	1.440	1	1.44	1

1425 d(Å) – d-spacing in Ångstroms. Intensities are relative to the intensity of the 7.2 Å

1426 reflection. [#]Overlaps with a major pentlandite reflection. Abbreviations: B – broad, U –

1427 unresolved peak or shoulder. S – serpentine. 1T and 1M refer to two polytypes of

1428 cronstedtite.

1429

1430

1431

1432

1433

1434 **Table 2**. Published d-spacings (Å) and corresponding hkl planes for the "060" XRD region
1435 of selected Fe- and Mg-rich serpentine group minerals. Note, only reflections with relative
1436 intensities >20% relative to the most intense reflection for that diffraction pattern are listed.

1437

Mineral	d-spacing (hkl)
[1]Greenalite 1T	1.614 (060), 1.575 (061,331)
[6]Cronstedtite 1T	1.585 (030), 1.547 (031)
[7]Cronstedtite 1M	1.589 (-331), 1.583 (-134), 1.550 (-332)
[2]Odinite	1.552 (060)
[3]Berthierine ("Chamosite H")	1.552 (060), 1.516 (06I), 1.471 (204)
[4]Berthierine ("Ferrous chamosite")	1.560 (060), 1.523 (06I)
[5]Amesite 2H$_2$	1.529 (060,330)
[6]Chrysotile 2Or$_{c1}$	1.533 (060), 1.503 (208)
[6]Chrysotile 2M$_{c1}$	1.531 (060)

1438 [1]Guggenheim et al. (1982), [2]Bailey 1988b, [3]Brindley 1951, [4]Brindley and Youell (1953),
1439 [5]Bailey 1988a, [6]Wicks and O'Hanley 1988, [7]Hybler 2006, [8]Hybler 2014.

1440 =====

1441

1442

1443   **Table 3**. Percent weight loss measured by TG as a function of temperature for three Aguas

1444   Zarcas and one Murchison sample. Weight-loss ranges are after Garenne et al. (2014) and

1445   discussed in the text.

1446

Sample	RT – 200 °C	200 – 400°C	400 – 770 °C	770 – 900 °C	Total	200 – 900 °C	900 – 1000 °C
AZMF6	1.6	2.3	6.4	0.6	10.9	9.3	0.5
AZMF7	1.6	3.3	7.1	0.9	12.8	11.3	0.7
AZMF2	2.3	2.4	8.9	0.8	14.4	12.1	0.3
Murchison	2.0	3.9	7.2	1.1	14.2	12.2	0.3
[1]Murchison	2.7	3.5	7.3	1.9	15.4	11.6	

1447   [1]From Garenne et al. 2014, Table 1.

1448

1449

1450

1451

1452

1453

1454

Table 4. Representative WDS analyses in wt% of the matrix materials. Dark, Medium, and Bright refer to their relative brightness in the BSE image in Fig. 11.

1457

Element (wt%)	#2121_5 Bright Blade (1)	#2121_5 Dark (1)	#2121_7 Dark (4)	#2121_7 Medium (4)	#2121_7 Bright (3)	#2121_8 Dark (6)	#2121_8 Bright (2)
Mg	4.6	16.2	18.8±0.6	9.9±0.7	6.5±1.2	13.5±0.5	9.3±0.3
Si	3.8	17.1	18.9±0.4	12.7±0.5	2.5±0.4	14.0±0.7	12.9±0.9
Al	1.12	1.06	0.65±0.01	1.69±0.11	0.77±0.72	1.42±0.10	1.85±0.35
Ca	0.01	0.05	0.12±0.02	0.71±0.3	0.31±0.08	0.09±0.01	0.08±0.01
Fe	44.1	12.3	8.6±0.4	24.4±2.2	38.0±2.5	20.5±1.1	26.2±3.8
S	14.3	0.88	0.94±0.18	2.54±0.48	10.3±0.3	5.2±0.7	3.6±0.9
Ni	1.69	0.22	0.67±0.05	1.43±0.48	2.4±1.8	0.09±0.03	0.06±0.03
O	21.6	34.9	37.5±0.5	30.8±0.3	20.9±0.2	32.3±0.8	30.3±0.1
tot	91.5	84.4	87.1±0.4	85.3±0.9	84.1±0.7	87.8±0.7	85.0±2.1

1458

1459

1460

1461